

Submesoscale Dynamics near a Seamount. Part I: Measurements of Ertel Vorticity

ERIC KUNZE AND THOMAS B. SANFORD*

School of Oceanography, University of Washington, Seattle, Washington

(Manuscript received 29 July 1992, in final form 28 December 1992)

ABSTRACT

The prevailing view that submesoscale fluctuations (horizontal wavelengths less than a few kilometers and vertical wavelengths less than a few hundred meters) are dominated by internal gravity waves is tested by measuring Ertel's potential vorticity, $\Pi = (f + \nabla \times \mathbf{V}) \cdot \nabla B$, where the buoyancy $B = -g\delta\rho/\rho_0$. Unlike geostrophic or nonlinear Ertel vorticity-carrying motions, internal waves have no Ertel vorticity fluctuations. Velocity and temperature profile surveys beside Ampere Seamount reveal appreciable Ertel enstrophy, and thus a significant non-internal-wave component, on horizontal wavelengths of 6–15 km and vertical wavelengths of 50–380 m. The twisting terms are negligible and the relative vorticities less than $0.2f$, so the anomalies are in geostrophic balance.

It is unlikely that the anomalies arise from stirring of the large-scale isopycnal gradients of stretching and planetary Ertel vorticity as this would require stirring lengths of thousands of kilometers. The most likely source appears to be forcing at the seamount, but generation by (i) dissipative 3D turbulence in the pycnocline or (ii) detrainment of the winter mixed layer cannot be absolutely ruled out. It remains to determine whether the coexistence of internal wave and Ertel vorticity-carrying fluctuations characterizes smaller scales ($\lambda \leq 50$ m, $\lambda_H \leq 5$ km) in the deep ocean away from topography as well.

413
692
94-08329
22p

94 3 14 049

Distinction Statement A
Approved for public release
Distribution Unlimited

1. Introduction

Ocean fluctuations with vertical wavelengths less than a few hundred meters and horizontal wavelengths less than a few kilometers are usually interpreted as internal gravity waves (e.g., Garrett and Munk 1979). However, Holloway (1983) and Müller (1984) have questioned this view, pointing out that geostrophic and nonlinear Ertel vorticity-carrying motions can coexist on these same scales. The generalization of geostrophic motion to include high Rossby number $|\zeta|/f$ and high Froude number $|V_z|/N$ describes the part of the flow that carries Ertel vorticity (Müller 1984). Manifestations of Ertel vorticity-carrying dynamics have been referred to as blobs, lenses, blini, pancake eddies, geostrophic turbulence, and stratified turbulence in the literature. These motions are distinct from three-dimensional dissipative turbulence in that their diapycnal motions are weak and they do not mix fluid across isopycnals. The relative contributions of internal waves and Ertel vorticity-carrying fluctuations in the ocean may have important consequences for understanding the high-horizontal-wavenumber end of the potential

enstrophy cascade, horizontal mixing, and the production of dissipative turbulence.

The challenge for observationalists is to distinguish between internal wave and Ertel vorticity-carrying fluctuations in the sea. These two kinds of motion have several distinguishing properties. Internal waves have intrinsic frequencies $f < \omega < N$, where f is the Coriolis frequency and N the buoyancy frequency, while Ertel vorticity-carrying fluctuations are subinertial ($\omega \ll f$). This allows identification of large-scale fluctuations (which are little affected by advective nonlinearity) using moored time series measurements. However, smaller scales become increasingly Doppler smeared. For example, Briscoe (1977), Müller et al. (1978), and Eriksen (1978) could not identify the dynamics of fine-structure in the internal wave continuum band ($f \ll \omega_E \ll N$) of amplitude 2 cm s^{-1} and vertical wavelength ≤ 10 m. This finestructure contained more kinetic energy than could be explained by the observed potential energy assuming linear internal wave dynamics. Kunze et al. (1990) confirmed this result and reported excess potential energy in the near-inertial band ($\omega_E \approx f$). They argued that this could be explained by near-inertial waves being Doppler smeared across the continuum band and continuum internal waves being Doppler smeared into the near-inertial band without having to invoke non-internal wave dynamics. This conjecture is supported by the work of Sherman and Pinkel (1991) who transformed CTD profile time series of finescale strain ξ_z (where ξ is the isopycnal displacement) into isopycnal-following coordinates, thereby removing the

* Also at Applied Physics Laboratory, University of Washington, Seattle, Washington.

Corresponding author address: Dr. Eric Kunze, School of Oceanography, WB-10 University of Washington, Seattle, WA 98195.

effects of vertical Doppler shifting and aliasing. In this "semi-Lagrangian" frame, most of the finescale strain fluctuations were attributable to low-frequency internal waves. Anderson and Pinkel (1993) reach the same conclusion for finescale shear.

As its name suggests, an unambiguous property of Ertel vorticity-carrying flow is Ertel's (1942) potential vorticity, which will be defined here as the dot product of the absolute vorticity ($2\Omega + \nabla \times \mathbf{V}$) and the gradient of the buoyancy $\nabla(\bar{B} + b)$

$$\Pi = (2\Omega + \nabla \times \mathbf{V}) \cdot \nabla(\bar{B} + b), \quad (1)$$

where the planetary vorticity, $2\Omega = (0, 2\Omega \cos(\text{lat}), 2\Omega \sin(\text{lat})) = (0, f \cot(\text{lat}), f)$, and the buoyancy $\bar{B} + b = -g\delta\rho/\rho_0$ has been split into a large-scale background $\bar{B}(z)$, which depends only on depth, and submesoscale anomalies $b(x, y, z, t)$. Neglecting both the horizontal gradients of vertical velocity, w_x and w_y , and the meridional component of the planetary vorticity $2\Omega \cos(\text{lat})$ as compared to the vertical shears, u_z and v_z , (1) can be expanded into a background plus linear and nonlinear perturbations

$$\begin{aligned} \Pi = & \underbrace{f\bar{N}^2}_{(i)} + \underbrace{f b_z}_{(ii)} + \underbrace{(v_x - u_y)\bar{N}^2}_{(iii)} \\ & + \underbrace{(v_x - u_y)b_z}_{(iv)} - \underbrace{b_x v_z}_{(v)} + \underbrace{b_y u_z}_{(vi)}, \end{aligned} \quad (2)$$

where subscripts denote derivatives and $\bar{N}^2 = \bar{B}_z$ is the background buoyancy frequency profile. The background Ertel vorticity (i) involves only the large-scale stratification $\bar{B}(z)$ and the planetary vorticity f . The linear perturbation comprises buoyancy-gradient anomalies (vortex stretching) (ii) and relative vorticity (iii). Nonlinear Ertel vorticity anomalies arise from coupling of vertical buoyancy-gradient anomalies and relative vorticity (iv) and the twisting terms, (v) and (vi), which involve horizontal vorticities (vertical shears) and horizontal buoyancy gradients.

Term (ii) scales as the strain ξ_z , term (iii) as the vorticity Rossby number $R_\zeta = \zeta/f$, term (iv) as $R_\zeta \xi_z$, while terms (v) and (vi) scale as the Froude number squared $\text{Fr}^2 = U_z^2/N^2 = (u_z^2 + v_z^2)/N^2$. If the strain ξ_z , Rossby number $|\zeta|/f$, and Froude number U_z/N are small, the motion is geostrophic. Thermal wind then implies

$$\nabla_H^2 b_z = f \xi_z \Rightarrow \frac{f b_z}{\bar{N}^2 \xi_z} = \left(\frac{f k_z}{\bar{N} k_H} \right)^2 = \frac{1}{R_L} = \frac{\text{PE}}{\text{KE}}, \quad (3)$$

where k_H and k_z are horizontal and vertical wavenumbers, and PE and KE are the available potential and horizontal kinetic energies (Kunze 1993). From (3), it is clear that the vortex-stretching (ii) and relative vorticity (iii) terms have the same sign (Hoskins et al. 1985), and their ratio is proportional to the energy ratio PE/KE and a normalized aspect ratio $R_L = (N k_H /$

$f k_z)^2$ (length-scale Burger number) for geostrophic flow.

For high Rossby numbers ($N/f > |\zeta/f| \gg 1$), earth's rotation is unimportant and Ertel vorticity-carrying motion can be described as cyclostrophic or as stratified turbulence (Riley et al. 1981; Lilly 1983). Müller (1984) coined the term "vortical mode" to describe Ertel vorticity-carrying fluctuations at all Rossby and Froude numbers. We shall refer to them as Ertel vorticity-carrying dynamics in this paper.

Internal waves have no Ertel vorticity fluctuations because they propagate reversibly and the Ertel vorticity of a water parcel can only be modified by irreversible processes (Pedlosky 1979; Haynes and McIntyre 1987). For example, Lelong and Riley (1992) have shown that weak triad wave-wave and wave-vortex interactions do not modify Ertel vorticity. Vortices appear in numerical simulations of forced "internal waves" (Riley et al. 1981; Staquet and Riley 1989; Herring and Metais 1989) only if the forcing directly induces Ertel vorticity anomalies: Herring and Metais (1989) found that a numerically simulated field of random internal waves without Ertel vorticity forcing did not develop Ertel vorticity-carrying motions.

Measuring finescale Ertel vorticity is a daunting undertaking. Relative vorticity and nonlinear twisting can contribute significantly on the submesoscale (e.g., Pollard and Regier 1992), requiring measurements of horizontal gradients of u , v , and b , which are difficult to estimate reliably in the ocean. Müller et al. (1988) attempted to determine the linear Ertel vorticity perturbation, $f\bar{N}^2(\xi_z + \zeta/f)$, where $\xi_z = b_z/\bar{N}^2$, using the IWEX trimooring data to estimate relative vorticity ζ and horizontal divergence ∇ —from which they determined the strain.

$$\xi_z = \int w_z dt = - \int \nabla dt$$

—for horizontal separations of 5–1000 m. Unfortunately, a three-point array cannot distinguish vorticity and divergence if the dominant signal is from scales at or smaller than the array as is the case in the ocean (Lien and Müller 1992b). Furthermore, for horizontal separations less than 100 m, internal wave isopycnal slopes tilt horizontal vorticity (vertical shear) into vertical vorticity enough so that the linear Ertel vorticity is not a reasonable approximation for the total Ertel vorticity. Thus, Müller et al.'s (1988) conclusion that they identified Ertel vorticity finestructure is not tenable.

In this paper, we will look for submesoscale Ertel vorticity anomalies in two velocity and temperature profile surveys collected adjacent to Ampere Seamount. Ampere is a bank rising to within 53 m of the surface at 35°03.5' N, 12°52.2' W in the eastern North Atlantic (Fig. 1). Its eastern flank is relatively steep (slope 0.15; critical reflection frequency 7f) and western flank more gentle (slope 0.03; critical frequency 1.3f). This site

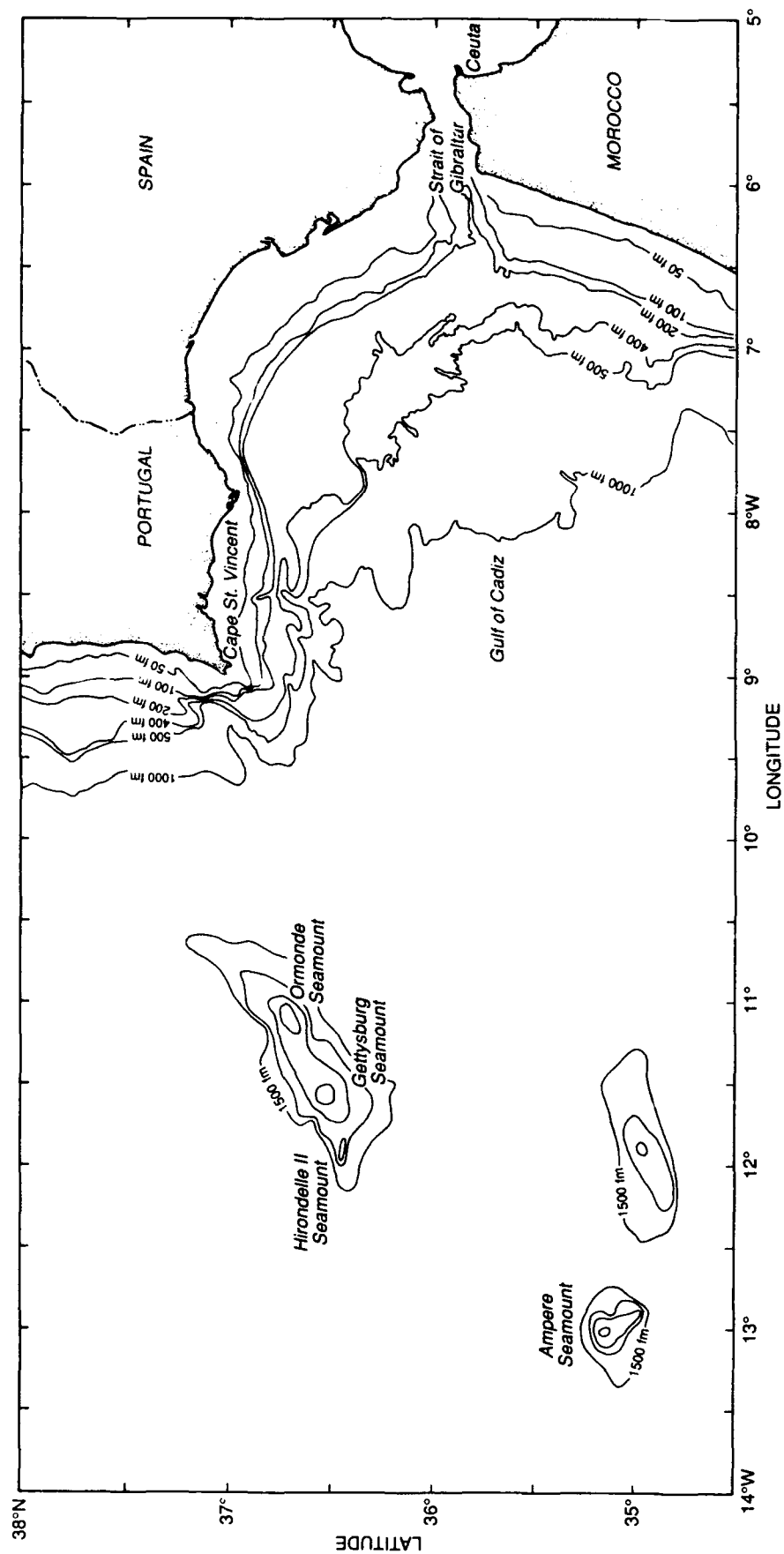


FIG. 1. Bathymetry in fathoms for the eastern North Atlantic showing the location of Ampere Seamount at 35°04'N, 12°52'W. The summit rises to within 53 m of the surface.

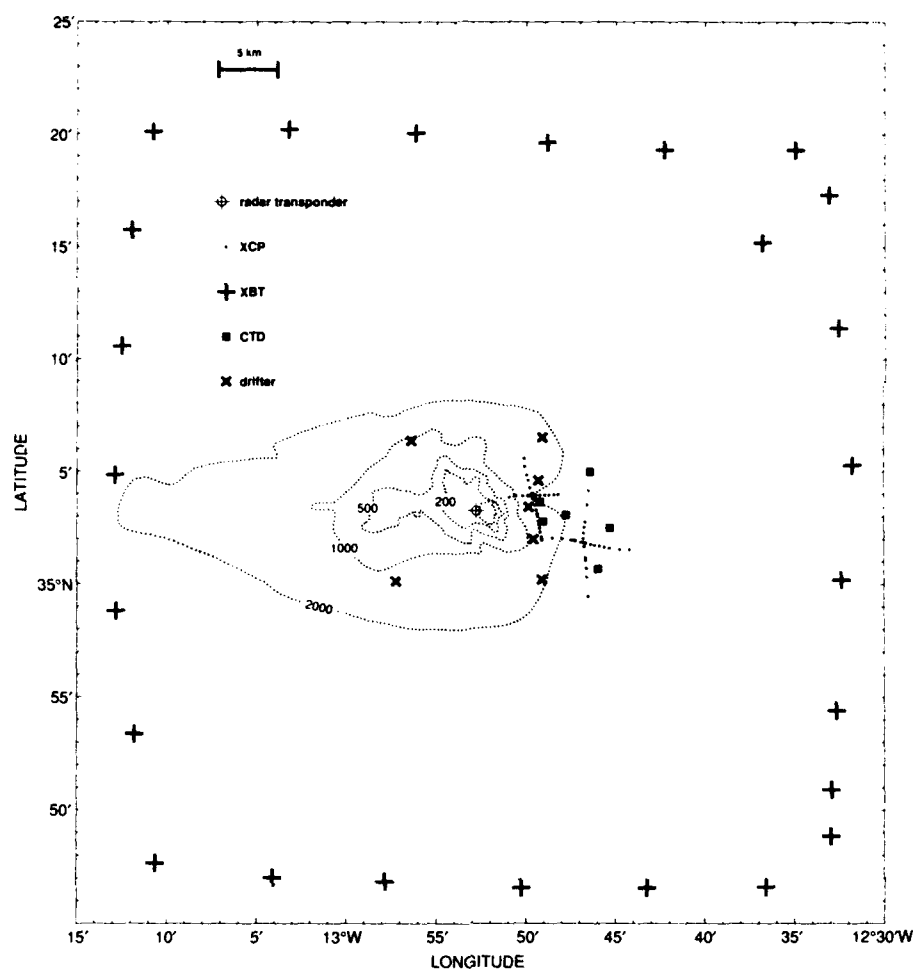


FIG. 2. Sampling around Ampere Seamount includes an XBT box survey around the seamount, seven drifter deployments, two cross-shaped XCP surveys, and six CTD casts. Bathymetry is in meters. The XCP surveys on the eastern flank contain 27 and 28 profiles with spacings of 0.3–1 km.

was chosen because it was thought that the likelihood of finding an Ertel vorticity signal would be greater in the vicinity of topography where boundary mixing and flow separation might produce shed eddies in the wake (Armi 1978; D'Asaro 1988b; Geyer and Signell 1990; Signell and Geyer 1991). We also examine the thermal wind balance and the ratio of horizontal divergence to relative vorticity.

Since the inception of this project, Lien and Müller (1992a) have developed a complete set of consistency relations in terms of vertical and horizontal wavenumbers for distinguishing linear internal waves and geostrophy. A companion paper (Kunze 1993) investigates the dependence of the energy ratio (or energy Burger number) PE/KE on the normalized aspect ratio (or length-scale Burger number) $(N\lambda_z/f\lambda_H)^2$ in this data. The observations are compared with the expected relationships for internal waves and geostrophy (Kunze et al., 1990; D'Asaro and Morehead 1991; Lien and Müller 1992a). The theoretical relations are used to

partition energy between internal waves and geostrophy. These results are consistent with the conclusions of this paper in that geostrophic and internal wave fluctuations are shown to coexist on the same scales next to Ampere Seamount, but the Burger number approach is able to probe smaller horizontal scales.

2. Measurements

The measurements consist of an XBT box survey 60 km on a side centered on the seamount, seven drifter deployments within 10 km of the summit, two cross-shaped expendable current profilers (XCP) surveys, and six CTD casts on the eastern flank (Fig. 2). The drifters were drogued to follow the average flow between 100 and 200 m depth using a high-drag line in that depth range and a low-drag line to the surface (Drever 1993, personal communication). They were tracked during 6–10 September 1988 by mooring a

radar transponder on the summit, then steaming the ship from one drifter to the next to get range and bearing of the transponder. Range is accurate to ± 200 m and bearing to $\pm 2^\circ$ (or 350 m at 10-km range). By comparison, Loran-C positioning at Ampere was only good to one kilometer.

The XBT box exhibited no large-scale impinging geostrophic flow in excess of the expected ± 5 cm s $^{-1}$ tidally induced noise. However, the drifters revealed subinertial flow in the near field. On the northern flank of the seamount and extending east in what resembles an interior boundary layer, the drifters moved eastward with average speeds of 5–7 cm s $^{-1}$ (Fig. 3). Tidal fluctuations of ± 5 cm s $^{-1}$ were also primarily in the east velocity component. On the eastern flank, motion was weak and random for the first three days, suggesting a stagnation point. Based on the lateral shear of $\geq 0.3f$ on the northeastern flank of Ampere Seamount (Fig. 3), flow separation and eddy shedding were thought most likely to occur there. Consequently, the first cross-shaped finescale XCP survey was conducted in the near-field shear zone on the afternoon of 8 September. The second survey was made ~ 5 km to the southeast on the afternoon of 9 September (Fig. 2). Six CTD casts to a depth of 2000 m were also made on the eastern flank to determine the local T , σ_θ relation. During the course of the second XCP survey, the drifters on the eastern flank accelerated to the south, reaching speeds of ~ 10 cm s $^{-1}$. This is reflected in the southward drifter velocities on the southeast flank in Fig. 3. The cause of this acceleration is unknown, but may be related to seamount-trapped waves (Brink 1990).

The XCP surveys contained 28 and 27 probes with 12–14 XCPs in each leg and drop spacings of 0.3–1 km. The sampling sequence for both surveys was from west to east, then from south to north. The first survey was effectively 4 km in diameter and the second 7 km. Each survey was completed in under three hours in an effort to minimize aliasing of the spatial gradients by temporal variability. The crossings of the east–west and north–south legs were ~ 2 h apart. A full description of the XCP sampling and data can be found in Kennelly et al. (1989).

Expendable current profilers measure the horizontal velocity (u , v) electromagnetically relative to an unknown but depth-independent constant (that is, they measure the baroclinic flow) and temperature with an XBT thermistor. These quantities are sampled at 0.3-m intervals from the surface to ~ 1600 -m depth. The upper 50 m is contaminated by temporally aliased surface swell (Sanford et al. 1982) and will therefore be excluded from analysis. In the pycnocline, the oceanic signal typically falls below instrument noise for wavelengths smaller than 10 m. Therefore, standard pre-analysis XCP processing smooths the raw data with a 6-m triangular window every 3 m. The same smoothing and subsampling was applied to the XBT data. The XCP rms velocity error is ± 0.4 cm s $^{-1}$ and the tem-

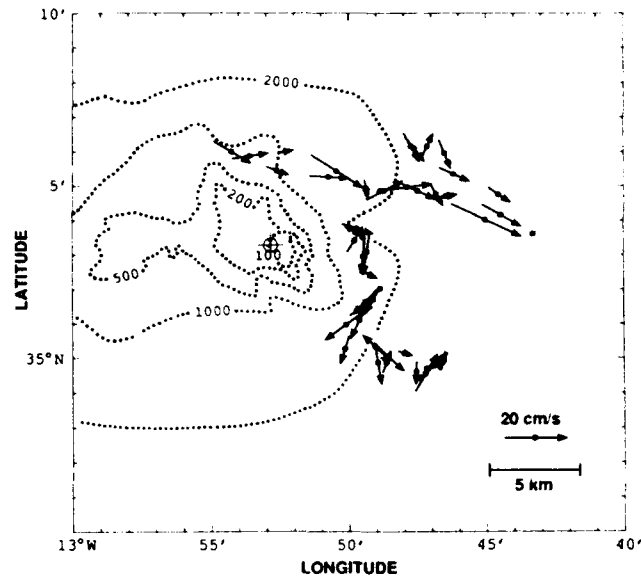


FIG. 3. Drifter velocities over 100–200-m depth around Ampere Bank for 6–9 September. On the northern flank and extending east, flow is eastward at 5–7 cm s $^{-1}$. On the eastern flank, flow is weak and random prior to 9 September. The first, or near-field, XCP survey (Fig. 2) was located in the strong shear on the northeast flank between the eastward flow and the “stagnation point.”

perature error $\pm 0.06^\circ\text{C}$. As we will be confining our attention to vertical wavelengths less than 400 m, the unknown barotropic velocity is of no concern.

We will use the survey data to compute vertical and horizontal gradients. The velocity error will result in shear errors of $\pm 10^{-4}$ s $^{-1} \approx 0.03N_\theta$ over 50 m in the vertical and $\pm 10^{-6}$ s $^{-1} \approx 0.013f$ over 4 km in the horizontal. The temperature error corresponds to $\pm 10^{-3}$ $^\circ\text{C m}^{-1}$ over 50 m equivalent to 10^{-6} s $^{-2} \approx 0.1N_\theta^2$ in N^2 and $\pm 10^{-5}$ $^\circ\text{C m}^{-1}$ over 4 km equivalent to 10^{-8} s $^{-2} \approx 0.05fN_\theta$ in b_z given the observed $\partial b/\partial T \approx -10^{-3}$ m s $^{-2}$ $^\circ\text{C}^{-1}$. Thus, as compared to $f = 8.3 \times 10^{-5}$ s $^{-1}$ and the 150–600-m depth-averaged buoyancy frequency $N_\theta \approx 3.5 \times 10^{-3}$ s $^{-1}$, instrument noise in velocity contributes smaller errors than temperature to an Ertel vorticity signal.

3. Estimating Ertel vorticity Π

a. Requirements

Estimating the different components of (2) and identifying Ertel potential vorticity anomalies requires determination of both horizontal and vertical gradients of u , v , and b . This can be accomplished with cross-shaped XCP surveys provided that (i) there is a tight T – S relation so that temperature can be used as a proxy for buoyancy, (ii) a valid separation can be made between the background \bar{N}^2 profile and the perturbation buoyancy gradient b_z , (iii) temporal variability during the 3 h of the surveys does not alias the horizontal gradients, and (iv) the surveys are horizontally coherent so that horizontal gradients can be estimated.

Figure 4 displays the $T-\sigma_\theta$ relation just east of Ampere based on the six CTD casts. The relation is tight for temperatures $T < 10.3^\circ\text{C}$ (depths greater than 1250 m) and for $11.7^\circ < T < 16.2^\circ\text{C}$ (150–600-m depth), allowing temperature to be used as a proxy for buoyancy in these depth ranges. Temperature is not a reliable measure of buoyancy in the salt-stratified thermostat between depths of 600 and 1200 m, a feature of the Mediterranean salt tongue, or in the upper 150 m ($T > 16.2^\circ\text{C}$) where water mass perturbations are evident. Therefore, the temperature–buoyancy relation can be reliably estimated only for 150–600 and 1250–1500 m.

The background buoyancy frequency profile $\bar{N}^2 = \bar{B}_z$ was determined from the mean temperature profile of the 25 XBTs, and therefore represents a 60-km scale average. Anomalies b_z are relative to this average profile. The XBT data did not extend below 750 m, so for the remainder of this paper, we shall confine our attention to the 150–600 m depth. In this range, $b(T) = T\partial b/\partial T$, with $\partial b/\partial T \approx -10^{-3} \text{ m s}^{-2} \text{ } ^\circ\text{C}^{-1}$ based on least-squares fits to the CTD data (Fig. 5). The XBT-average buoyancy frequency $\bar{N}(z)$ decreases from $3.6 \times 10^{-3} \text{ s}^{-1}$ at 150-m depth to $3.3 \times 10^{-3} \text{ s}^{-1}$ at 400 m, then increases to $3.7 \times 10^{-3} \text{ s}^{-1}$ at 600 m. The average buoyancy frequency over 150–600 m, $N_a = 3.5 \times 10^{-3} \text{ s}^{-1}$, will be used to normalize the Ertel vorticity terms.

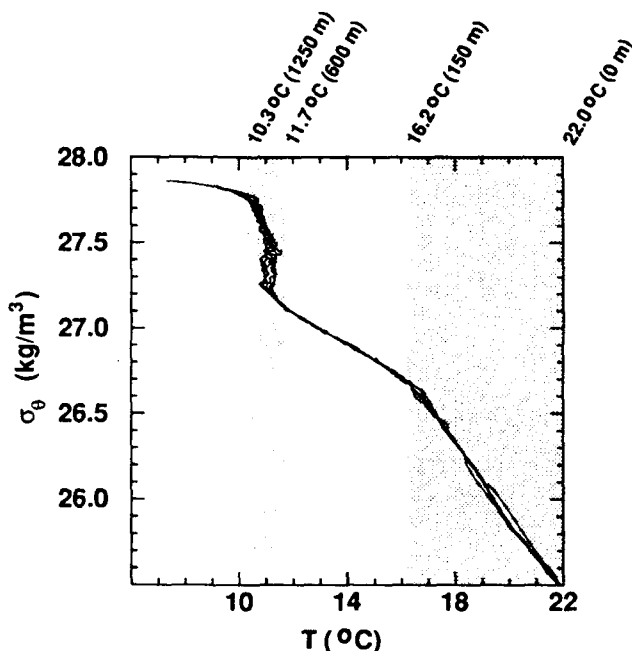


FIG. 4. Density σ_θ versus temperature T from the six CTD profiles collected on the eastern flank of Ampere. The $T-\sigma_\theta$ relation is tight for temperatures less than 10.3°C (depths greater than 1250 m) and between 11.7° and 16.2°C (150–600-m depth). Temperature cannot be used to infer buoyancy in the stippled ranges between 650 and 1200 m and above 150-m depth.

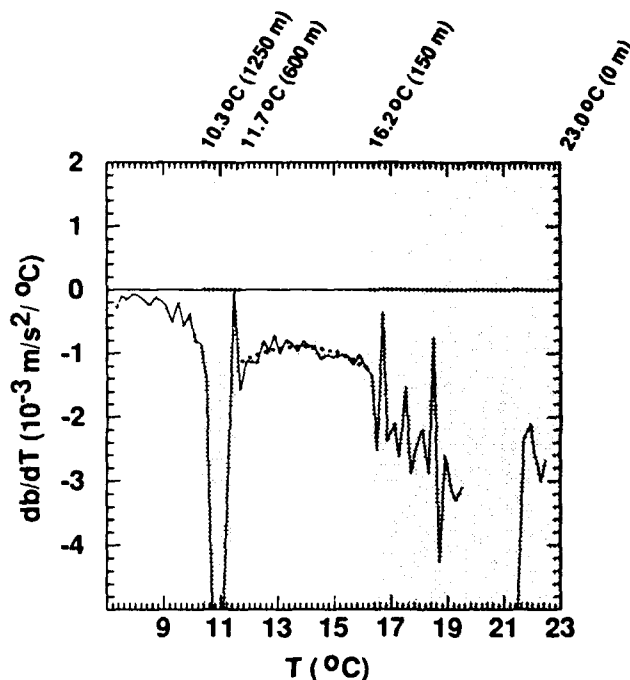


FIG. 5. The least-squares fit relation between temperature and buoyancy used to compute buoyancy frequency N^2 and stretching b_z in (2). Bootstrap standard deviations are denoted by stippling. Where the stippling extends over the entire range, the relation is not usable. This limits buoyancy estimates to depths 150–600 m and 1250–1600 m. The thick dotted curve corresponds to a least-squares cubic fit over $T = 11.7^\circ\text{--}16.2^\circ\text{C}$.

To accurately determine horizontal gradients, temporal variations during the 3-h surveys must not seriously alias the horizontal structure. Figure 6 displays vertical wavenumber spectra of the sums and differences of velocity profiles taken at the same location (within 0.5 km) but 2 h apart. If temporal variation was small, the “difference” spectrum should lie well below the “sum” spectrum. For wavelengths larger than 50 m, the difference spectrum is a factor of 3–4 smaller than the sum spectrum, commensurate with the expected wavenumber-independent change for a Garrett–Munk (GM) internal wave field (Munk 1981). By comparison, for profile pairs taken 5 min and 0.5 km apart (not shown), the difference spectrum lies below the sum for vertical wavelengths as small as 30 m. Therefore, the equipartition of energy between difference and sum spectra at wavelengths smaller than 50 m in Fig. 6 is due to temporal variability. Subsequent analysis will involve making survey fits that filter out the smaller horizontal wavelengths (higher frequencies) responsible for much of this temporal variability. Simulations using the GM model, low-pass filtered to remove the high horizontal wavenumbers suppressed by these fits, indicate that temporal contamination of the fits will be a factor of 2–3 smaller than the raw differences in Fig. 6. Thus, temporal contamination will be about 10% for $\lambda_z \geq 50$ m. Vertical wavelengths smaller

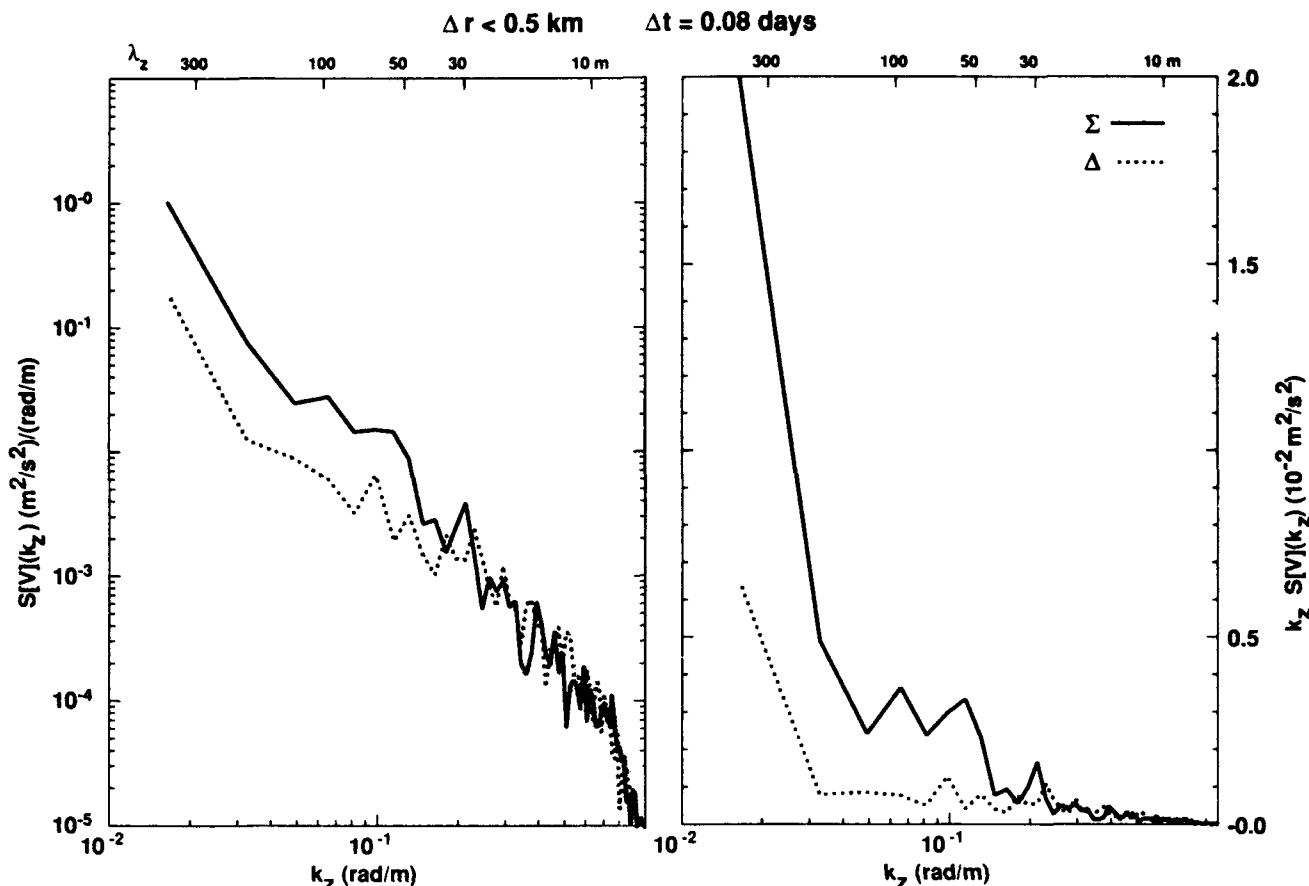


FIG. 6. Vertical wavenumber spectra for kinetic energy in the sums (Σ , solid) and differences (Δ , dotted) of profile pairs taken at the same position (within 0.5 km) but 2 h apart. The spectra are presented in both log-log (left) and variance-preserving (right) formats. Instrumental noise is indicated by stippling and is smaller than the thickness of the lines except at high wavenumbers ($\lambda_z < 10$ m) in the log-log spectra. For wavelengths $\lambda_z > 50$ m, the sum spectrum exceeds the difference by factors of 3–4. At smaller wavelengths, there is equipartition between the sum and difference spectra.

than 50 m will be treated as unreliable for determining horizontal gradients, an assumption in agreement with the noise in the horizontal gradient estimates.

To illustrate that the surveys are horizontally coherent, Fig. 7 displays the east–west section of east velocity u , north velocity v , and vertical displacement $\xi = (T - \langle T \rangle) / \langle T_z \rangle$ from survey 2. Coherent fluctuations extend across all or most of the section down to wavelengths of ~ 50 m.

Because the surveys are horizontally coherent, we can estimate the horizontal gradients $\partial/\partial x$ from the east–west legs and $\partial/\partial y$ from the north–south legs using linear least-squares fits at each depth. The resulting gradients can be combined to determine dynamically relevant variables. By fitting over many points in the horizontal, we suppress measurement noise and the fluctuations in high horizontal wavenumber that contaminated the IWEX estimates (Müller et al. 1988; Lien and Müller 1992b), although a cross-shaped array is not optimal for reducing mutual contamination of relative vorticity and horizontal divergence (Lien 1992, personal communication; see appendix B).

Figure 8 displays (a) horizontal divergence $(u_x + v_y)/f$ and (b) relative vorticity $(v_x - u_y)/f$ profiles from survey 1 for several horizontal fitting ranges Δr bracketing survey center. As the fitting scale Δr increases, so does the number of profiles going into the fit (number shown at base of each profile). Therefore, the standard deviation (stippling) as determined by the bootstrap method (Efron and Gong 1983) diminishes. For example, at $\Delta r = 4.3$ km, the horizontal divergence and relative vorticity have significant fluctuations down to wavelengths of 50 m with rms values of 0.1–0.2 f , an order of magnitude larger than instrument noise but only a factor of 2 larger than unresolved oceanic noise $\sim 0.07 f$.

Horizontal buoyancy gradients, b_x and b_y , were estimated in a similar manner and combined with vertical shears, u_z and v_z , averaged over fitting scale Δr , to obtain the twisting terms $[(v)$ and (vi) in (2)]. This neglects contributions from subsurvey scales of the form $\langle (b_x - \langle b_x \rangle)(v_z - \langle v_z \rangle) \rangle$.

Inertially backrotating the velocity profiles to a common time before carrying out the fits did not alter

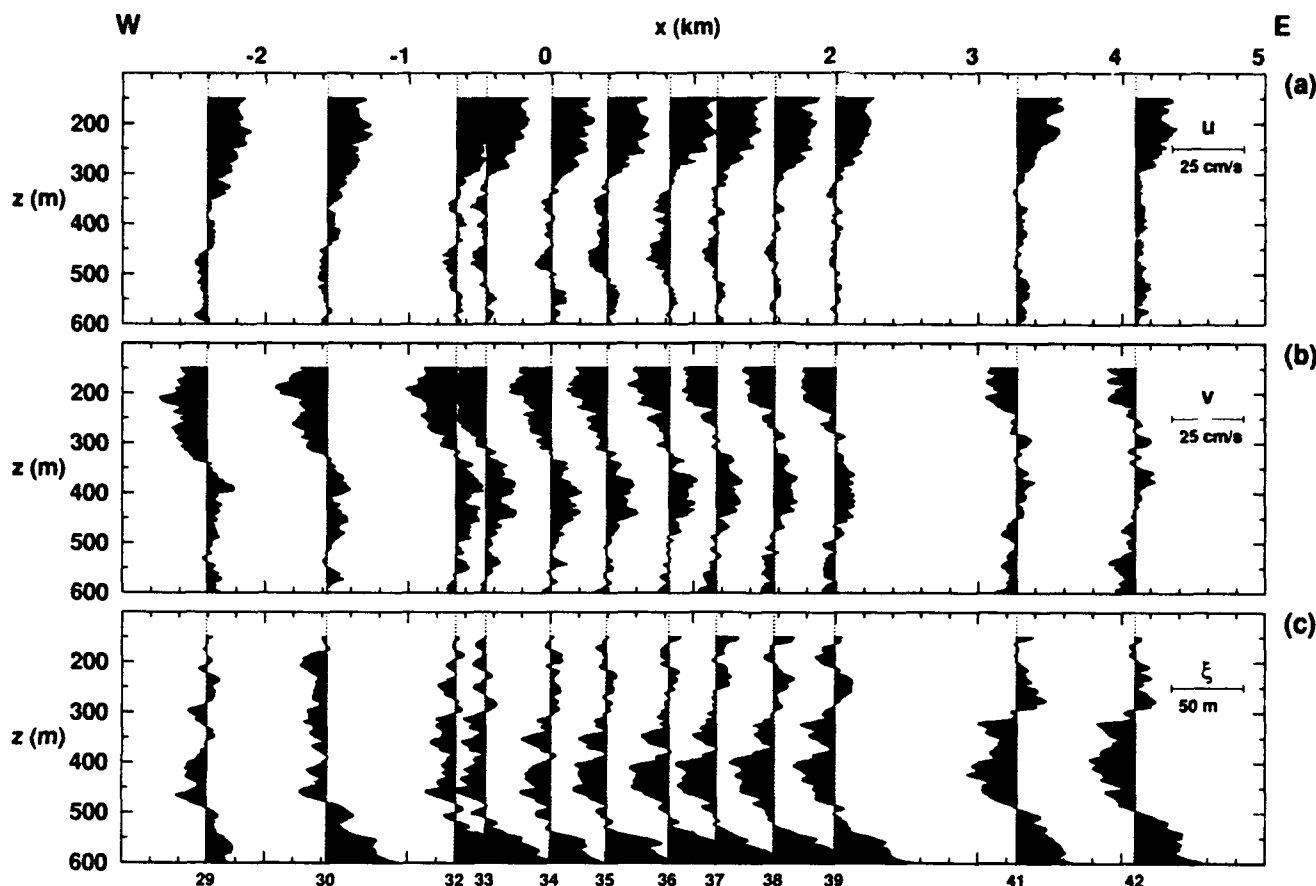


FIG. 7. Sample section of (a) east velocity u , (b) north velocity v , and (c) vertical displacement $\xi = (T - \langle T \rangle) / \langle T_z \rangle$ from the east-west leg of the second XCP survey. Drop numbers are indicated along the bottom axis. The dotted vertical lines are profile zeros. Structure down to vertical wavelengths of ~ 50 m can be traced across all or most of the section.

details of the vorticity and divergence profiles appreciably because of the short duration of the surveys (3 h). Likewise, transforming the u , v , and b profiles into isopycnal coordinates did not modify the estimates because isopycnal displacements on the scale of the surveys were small compared to the 50–400-m vertical wavelengths of interest.

b. Ertel vorticity profiles

With the ability to estimate relative vorticity, vertical shear, and buoyancy gradients, the Ertel vorticity (2) can be assessed. As will be shown (Fig. 10), the nonlinear terms are negligible. Therefore, profiles of the linear perturbation Ertel vorticity, $f b_z + \zeta \bar{N}^2$, are displayed in Fig. 9. The vertical buoyancy-gradient anomaly b_z for the vortex-stretching term $f b_z$ was averaged over the same fitting scale as relative vorticity. The linear perturbation Ertel vorticity has significant anomalies. For example, a 50-m wavelength feature with amplitude $\sim 0.5 f \bar{N}^2$ resides at 400-m depth for $\Delta r = 4.3$ km. Smaller amplitude fluctuations are apparent above and below this feature.

c. Spectra

The relative contributions of the various linear and nonlinear terms to the Ertel vorticity perturbation (2) are most clearly illustrated with vertical wavenumber spectra. Fourier transforms were applied to de-meaned profiles of 128 points (380 m) starting at 150-m depth and windowed at both ends with 10% \sin^2 tapers. The spectra are displayed in Fig. 10. Table 1 summarizes the rms contributions to the Ertel vorticity for vertical wavelengths greater than 50 m. For the 4- and 7-km fits, the nonlinear terms, ζb_z , $b_z v_z$, and $b_z u_z$, contribute little and are below oceanic noise. Since the Rossby number is less than 0.2 and the nonlinear terms less than $0.05 f \bar{N}_0^2$, any Ertel vorticity anomalies can be attributed to geostrophic motion. Likewise, any internal wave fluctuations will be linear.

The vortex-stretching $f b_z$ spectral level (thick solid) far exceeds that of the other Ertel vorticity terms. In survey 1, most of the vortex-stretching variance (rms magnitude $0.2 f \bar{N}^2$) is at 200- and 50-m wavelengths. Relative vorticity $\zeta \bar{N}^2$ (thin solid, Fig. 10a) also has most of its variance (rms magnitude $0.1 f \bar{N}^2$) at these wavelengths but is markedly weaker.

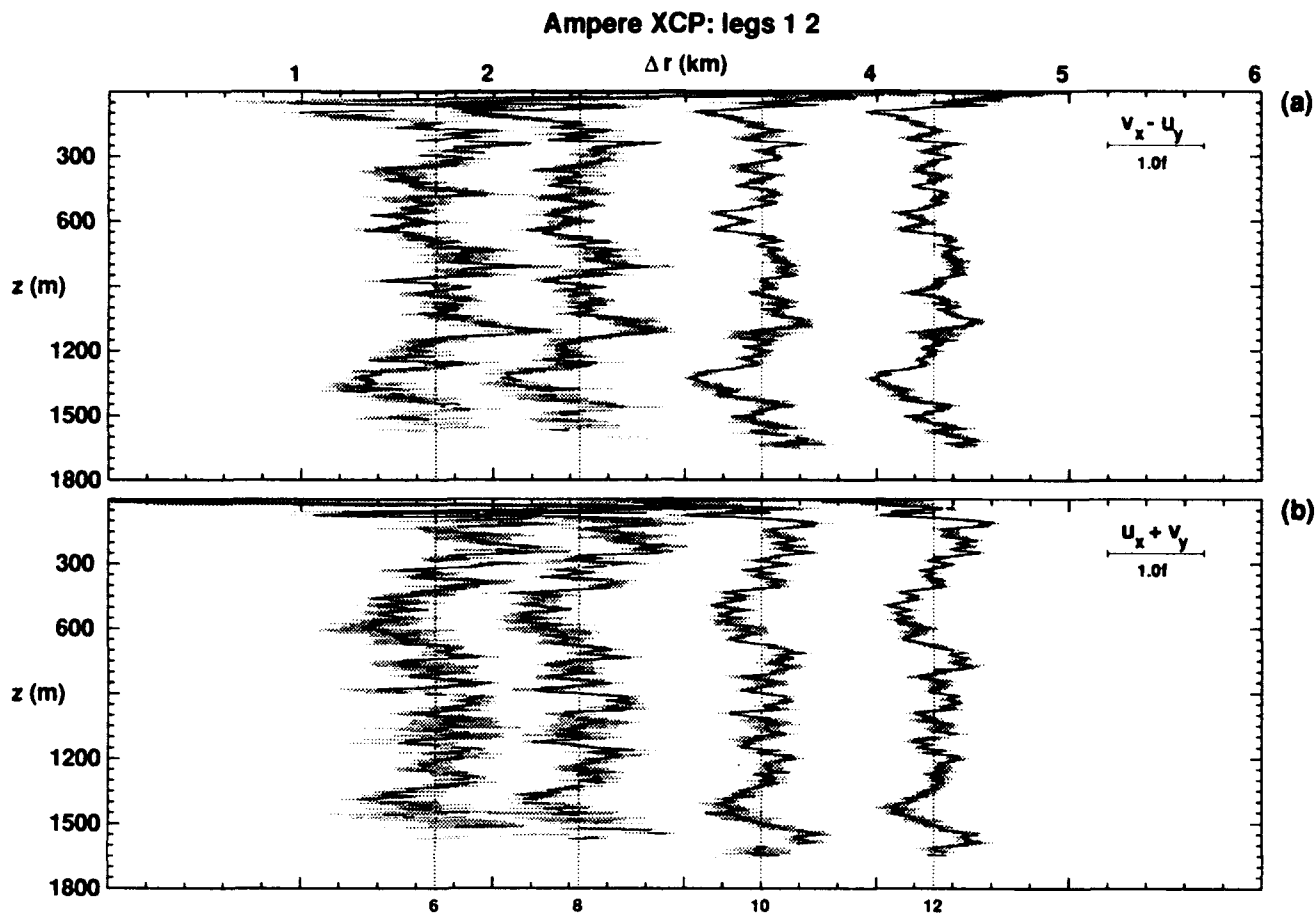


FIG. 8. Horizontal divergence $\nabla = (\nabla \cdot \mathbf{V}_H) = u_x + v_y$ (a) and relative vorticity $\zeta = (\nabla \times \mathbf{V}_H) = v_x - u_y$ (b) as functions of depth and fitting scale Δr based on horizontal least-squares linear fits to the velocity profile sections. The number of profiles going into the fit is marked along the bottom axis and the bootstrap standard deviations about the fits indicated by stippling. At fitting scales of 3.5–4.3 km, horizontal divergence and relative vorticity have significant fluctuations down to ~ 50 -m wavelengths with rms values of $0.2f$.

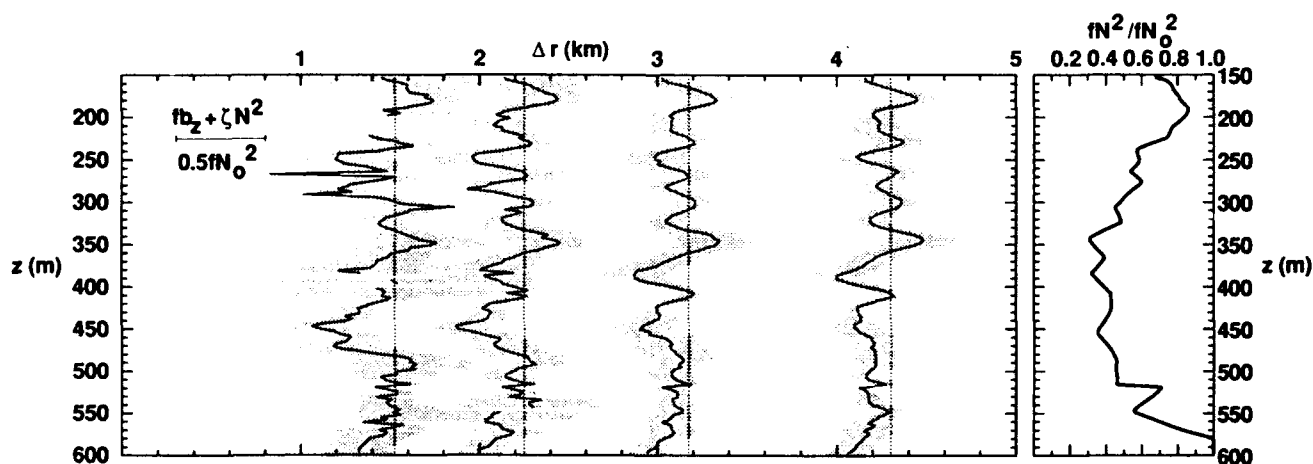


FIG. 9. Linear perturbation Ertel vorticity, $f b_z + \zeta N^2$, as a function of depth and fitting scale Δr from the near-field survey (left panel) in the upper depth range where the T - σ_θ relation is tight. The background Ertel vorticity $f N^2 / f N_0^2$ (right panel) is based on the mean XBT profile. The dotted vertical lines correspond to profile zeros and are located at the appropriate fitting scale. Bootstrap standard deviations are indicated by stippling. Estimates are not plotted if the standard deviation exceeds $1.5 f N^2$.

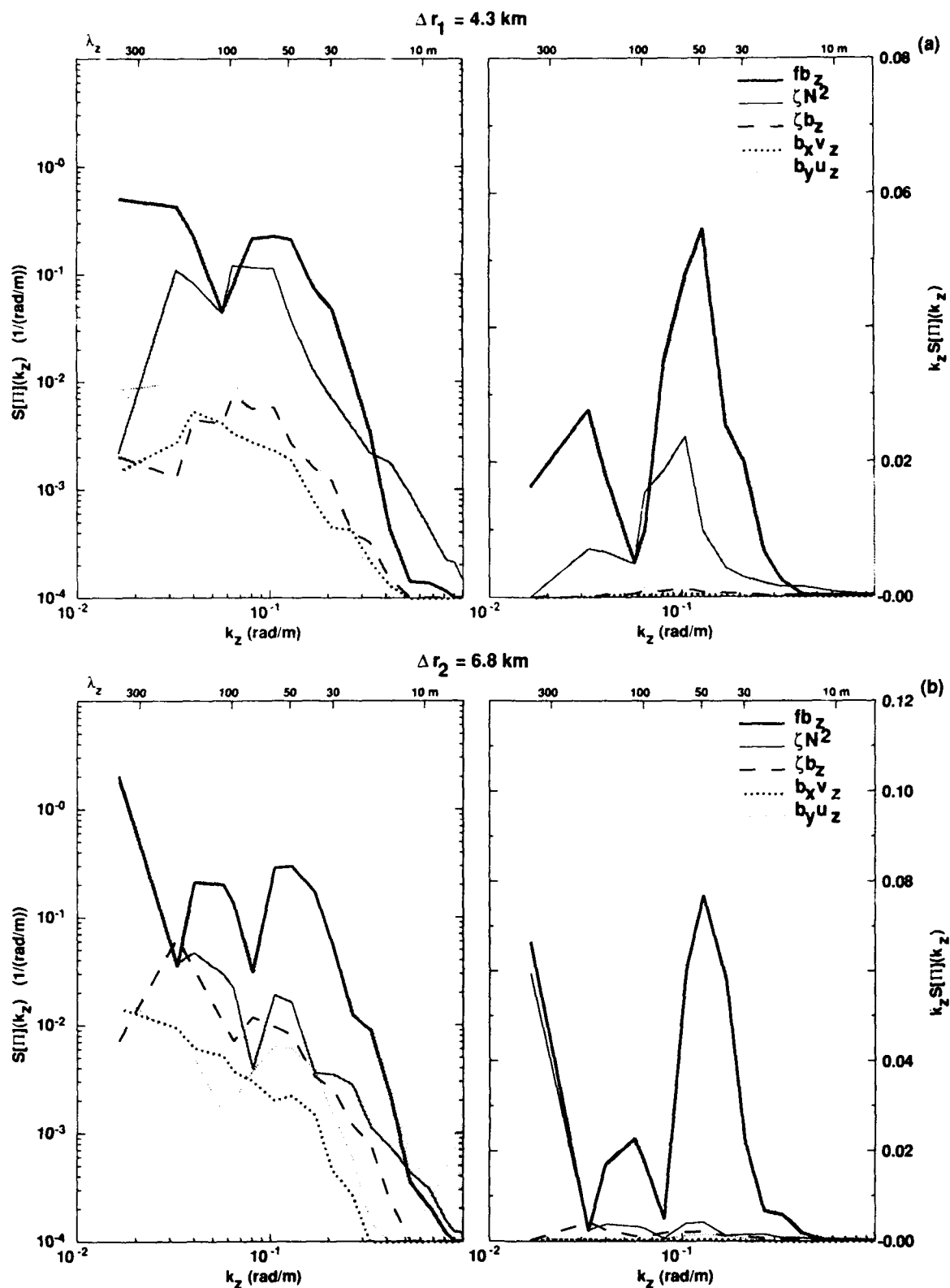


FIG. 10. Vertical wavenumber spectra of the two linear and three nonlinear components of the Ertel vorticity perturbation (normalized by fN_0^2 , $N_0 = 3.5 \times 10^{-3} \text{ s}^{-1}$) from survey 1 for a fitting scale $\Delta r = 4.3 \text{ km}$ (a) and survey 2 for a fitting scale $\Delta r = 6.8 \text{ km}$ (b). Spectra are presented in both log-log (left panels) and variance-preserving (right panels) formats. The shading about the vortex-stretching and relative vorticity curves denotes one standard deviation. Vortex stretching fb_z (thick solid) dominates except at the lowest resolved vertical wavenumber ($\lambda_z = 380 \text{ m}$) in survey 2 where vortex-stretching and relative vorticity levels are comparable. The nonlinear terms are negligible.

TABLE 1. Rms values of the perturbation terms of Ertel's potential vorticity (2) for depths 150–600 m and $\lambda_z = 50$ m scaled by $fN_z^2/\Delta z$ ($3.5 \times 10^{-3} \text{ s}^{-1}$). The GM model values (in parentheses) are larger for the first survey because the low-pass horizontal wavenumber filter includes higher wavenumbers.

	($\Delta r = 4.3$ km) survey 1 (GM)	($\Delta r = 6.8$ km) survey 2 (GM)	rms error
$f b_z + \zeta N^2$	0.22 (0.00)	0.31 (0.00)	0.10
$f b_z$	0.19 (0.45)	0.25 (0.20)	0.08
ζN^2	0.10 (0.45)	0.18 (0.20)	0.05
$\nabla^2 \Delta z$	0.22 (0.83)	0.10 (0.29)	0.05
∂_z	0.03	0.05	0.04
$b_z v_z$	0.02	0.03	0.05
$b_z u_z$	0.03	0.03	0.04

For survey 2 (fitting scale $\Delta r = 6.8$ km), the vortex stretching again dominates (Fig. 10b). Most of the vortex-stretching variance (rms magnitude $0.25 f N^2$) is at 380-, 140-, and 50-m wavelengths. The relative vorticity is much weaker at 110- and 50-m wavelengths, indicating an Ertel vorticity perturbation almost entirely associated with vortex stretching. However, at 380-m wavelength, the relative vorticity and vortex-stretching variances are comparable, so the signal could be due to internal wave or geostrophic motions.

Which of these is responsible can be determined by examining spectra of the linear Ertel vorticity anomaly, $f b_z + \zeta N^2$ (Fig. 11). For linear internal waves, vortex stretching and relative vorticity are equal and opposite ($f b_z = -\zeta N^2$) so that, if the relative vorticity was largely from internal waves, one would expect the variance of $f b_z + \zeta N^2$ to be reduced from that of $f b_z$. In contrast, $f b_z$ and ζN^2 are in phase for geostrophy (3), so geostrophic $f b_z + \zeta N^2$ variance will exceed $f b_z$ variance. Figure 11b reveals that $f b_z + \zeta N^2$ has greater variance than $f b_z$ at $\lambda_z = 380$ m in survey 2, signifying that the relative vorticity at this wavelength is associated with geostrophy. From (3), the corresponding horizontal wavelength should be ~ 15 km or roughly twice the size of the array. (Finding horizontal wavelengths larger than the array does not invalidate the analysis since the fits include contributions from all wavelengths larger than the array.) The vortex-stretching peaks at $\lambda_z = 110$ and 50 m have inferred horizontal wavelengths of 7 km and >4 km where the presence of some internal wave vorticity at 50-m vertical wavelength leads to potential underestimation of its horizontal wavelength. Likewise, in survey 1 (Fig. 11a), $f b_z + \zeta N^2$ exceeds vortex stretching at the peaks, signifying that the bulk of the relative vorticity is in phase with the vortex stretching and therefore associated with geostrophy. The corresponding horizontal wavelengths (3) at $\lambda_z = 200$ and 60 m are 12 and >3 km, respectively. The fractions of kinetic energy contributed by internal waves and geostrophy are considered further in section 3d and by Kunze (1993).

While vortex stretching greatly exceeds GM model levels (Fig. 12a), the vorticity spectra are roughly comparable except at $\lambda_z = 60$ –100 m in survey 1 and $\lambda_z = 380$ m in survey 2 (Fig. 12b). For this comparison, the high horizontal wavenumbers suppressed in the measurements by the least-squares fitting are filtered from the GM model with a simple boxcar low-pass filter with cutoff at $k_H = \pi/\Delta r$ (appendix A) (the GM spectra differ for the two surveys because of their different cutoff wavenumbers). Given the well-known factor of three variability in energy density on these scales (Munk 1981), more elaborate attempts to fit the GM model to the data are not justified.

d. Relative vorticity ζ and horizontal divergence ∇_H

Since the twisting terms are small, so that isopycnal tilting can be neglected, relative vorticity $\zeta = \nabla \times \mathbf{V}_H$ and horizontal divergence $\nabla = \nabla \cdot \mathbf{V}_H (= -w_z = -\xi_z)$ can also be used to distinguish linear internal waves and geostrophy since, (i) for geostrophic motions, horizontal divergence is weak compared to vorticity ($\nabla \ll \zeta$), while, for internal waves, $\langle \nabla^2 \rangle / \langle \zeta^2 \rangle = \omega^2 / f^2$ (Fofonoff 1969), so that (ii) near-inertial waves have comparable divergence and vorticity ($\nabla \geq \zeta$) and (iii) high-frequency internal waves have divergence exceeding vorticity ($\nabla \gg \zeta$). Thus, nonnegligible divergence indicates the presence of internal waves, and vorticity *in excess* of the divergence is ascribable to geostrophic motions. Relative vorticity and horizontal divergence are computed in the same way. This reduces concerns about different sampling and processing that arise when combining horizontal gradients of u and v with vertical gradients of buoyancy.

The observed relative vorticity and horizontal divergence fields are compared with GM model spectra for these quantities in Fig. 13. High horizontal wavenumbers, suppressed in the observations by fitting over the surveys, have been removed from the GM spectra with a boxcar filter (appendix A) for this comparison. Filtering has its greatest impact on the horizontal divergence, which is dominated by high-frequency, high-horizontal-wavenumber fluctuations in the GM model. More sophisticated filtering of the GM model to account for contamination of the vorticity by the divergence (Lien and Müller 1992b) is not warranted because this effect boosts the GM vorticity level by at most 10% above the divergence for vertical wavelengths $\lambda_z < 60$ m (Lien 1992, personal communication; see appendix B).

For the near-field survey 1 (Fig. 13a), the observations share with the low-pass horizontal-wavenumber-filtered GM model the tendency for (i) divergence to exceed vorticity at low vertical wavenumbers, and (ii) divergence and vorticity to be comparable at high vertical wavenumbers. However, the relative vorticity variance is twice the horizontal divergence variance for $\lambda_z = 60$ –100 m. Taking the vorticity in excess of

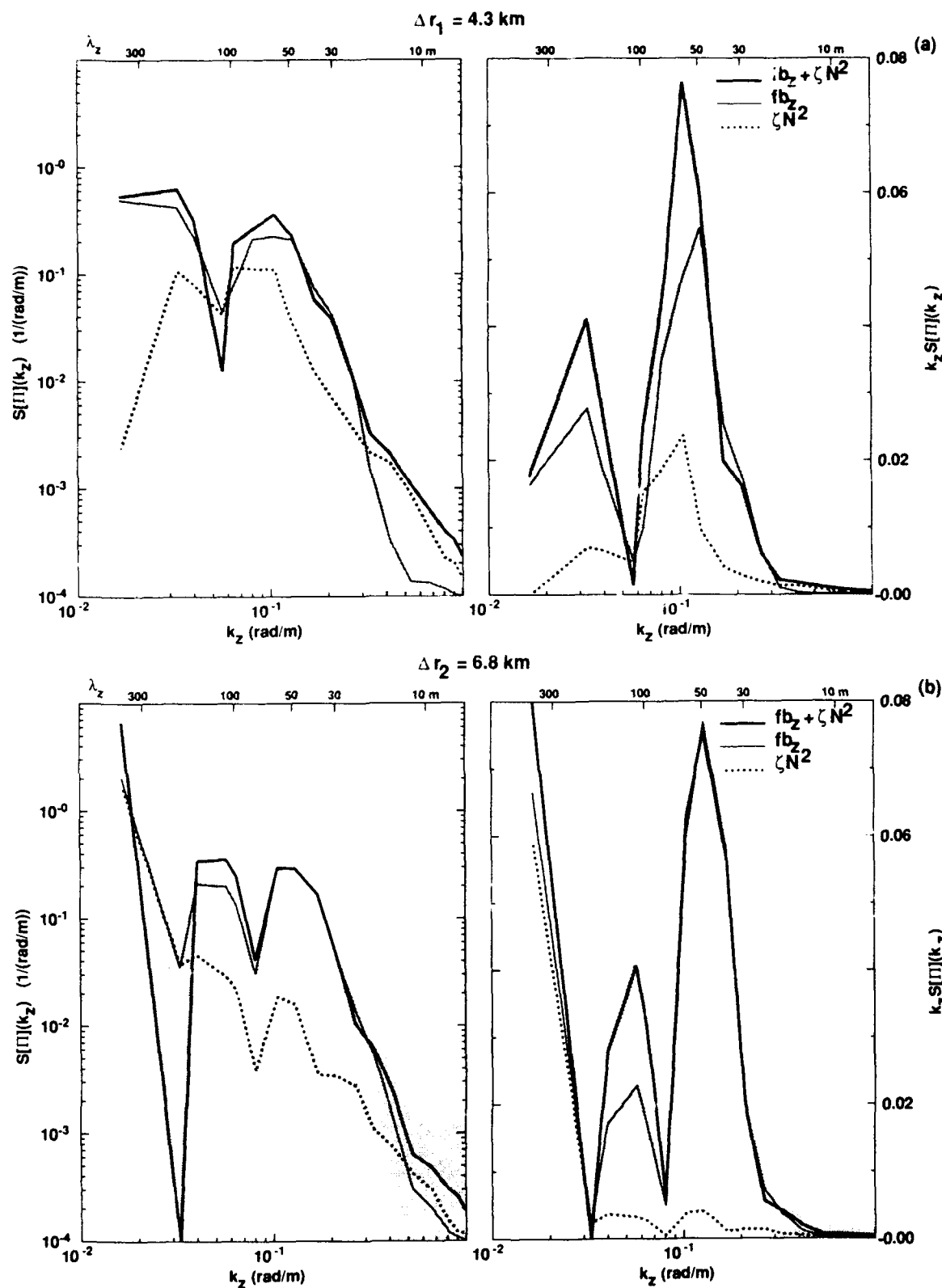


FIG. 11. Vertical wavenumber spectra of the linear Ertel vorticity anomaly, $f b_z + \zeta N^2$, vortex stretching $f b_z$, and relative vorticity ζN^2 normalized by $f N_0^2$ from survey 1, $\Delta r = 4.3 \text{ km}$ (a) and survey 2, $\Delta r = 6.8 \text{ km}$ (b). At the vortex-stretching spectral peaks (e.g., $\lambda_z = 60 \text{ m}$), the vortex-stretching plus relative vorticity spectra exceeds stretching alone, signifying that much of the relative vorticity is associated with submesoscale geostrophy, not internal waves.

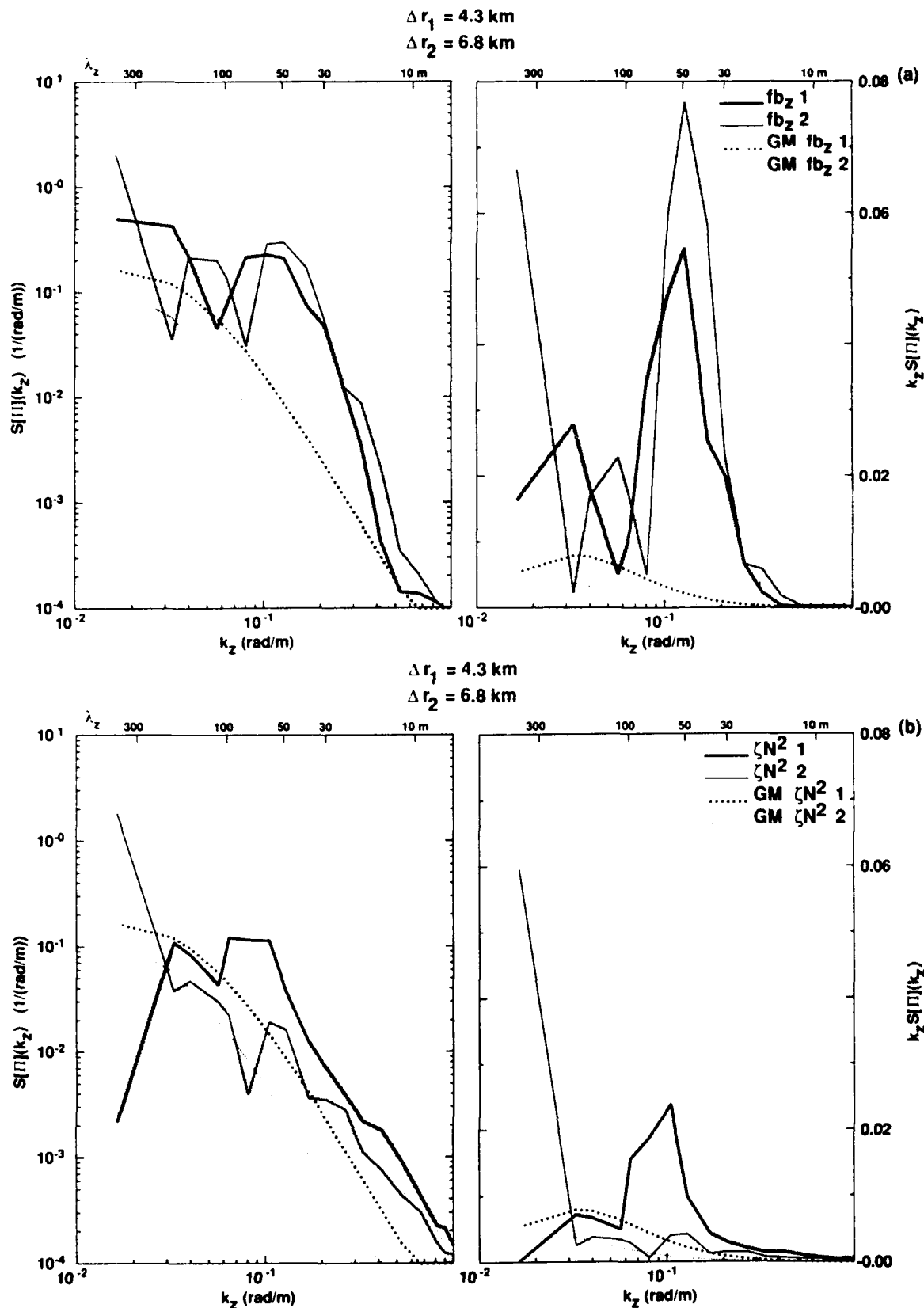


FIG. 12. Comparison of observed vertical wavenumber spectra for vortex stretching f/h_z (a) and relative vorticity ζN^2 (b) from survey 1 ($\Delta r = 4.3 \text{ km}$; thick solid) and survey 2 ($\Delta r = 6.8 \text{ km}$; thin solid) with the GM model spectra low-pass filtered to remove the high horizontal wavenumbers ($k_H > \pi/\Delta r$) suppressed by fitting over the surveys (dotted). All spectra have been normalized by f/N^2 . The observed vortex-stretching spectra (a) greatly exceed GM, while the observed relative vorticity spectra (b) have comparable levels and shapes to the GM model except for excess vorticity at 60–100 m wavelength in survey 1 and at the largest resolved wavelength ($\lambda_z = 380 \text{ m}$) in survey 2.

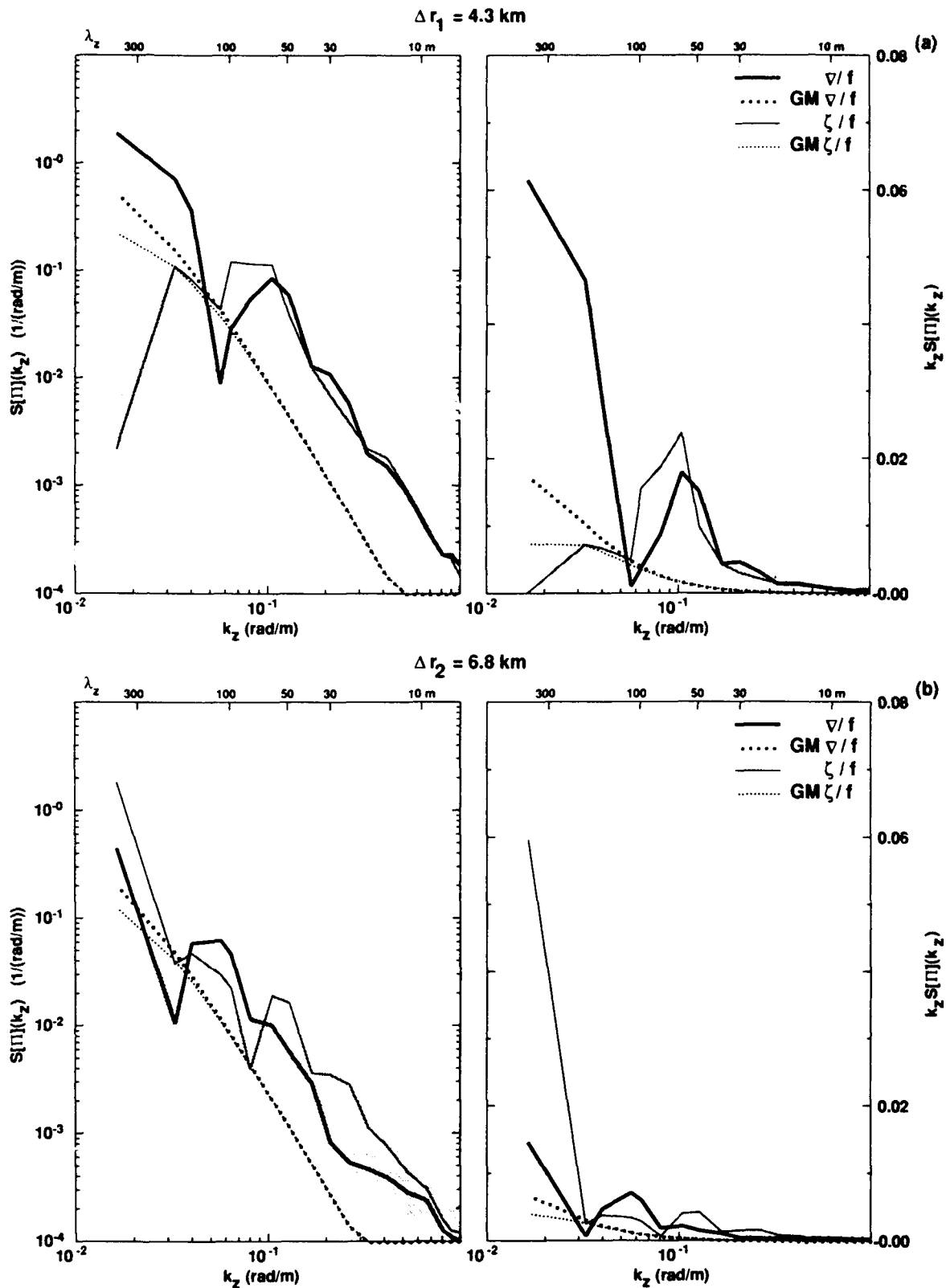


FIG. 13. Comparison of the measured vertical wavenumber spectra for horizontal divergence ($\nabla \cdot \mathbf{V}_H$)/ f (thick solid) and relative vorticity ($\nabla \times \mathbf{V}_H$)/ f (thin solid) from survey 1 for $\Delta r = 4.3$ km (a) and from survey 2 for $\Delta r = 6.8$ km (b), with GM model spectra low-pass filtered to remove high horizontal wavenumbers ($k_H > \pi/\Delta r$) suppressed by fitting over the surveys (thick and thin dotted). Bootstrap error bars (stippling) are less than the width of the curves in the variance-preserving format (right panels). Vorticity exceeds divergence consistent with geostrophic but not internal wave dynamics at $\lambda_z = 50$ –100 m in survey 1 and at the largest resolved wavelength ($\lambda_z = 380$ m) in survey 2.

the divergence to be geostrophic, this suggests that at least one-third of the kinetic energy in this band is associated with geostrophic motion. This is commensurate with the conclusion from Fig. 11a that the relative vorticity in this wavenumber band was largely geostrophic. Likewise, for survey 2 (Fig. 13b), relative vorticity exceeds horizontal divergence by a factor of 4 at $\lambda_z = 380$ m, signifying 0.5–4 times as much kinetic energy in geostrophic as internal wave motions at this wavelength. This is in agreement with the conclusion from Fig. 11b. For vertical wavelengths between 50 and 200 m, geostrophic kinetic energy is 0.05–2 times that in internal waves because the vorticity variance is twice the divergence variance.

e. Testing thermal wind

It is common to test for geostrophy by comparing the two terms of the thermal wind relation,

$$f\mathbf{V}_z = (-v_z, u_z) \quad \text{and} \quad \nabla_H b = (b_x, b_y).$$

For geostrophic flow, the ratio $\langle f^2 V_z^2 \rangle / \langle (\nabla_H b)^2 \rangle = 1$, while for internal waves,

$$\begin{aligned} \frac{\langle f^2 V_z^2 \rangle}{\langle (\nabla_H b)^2 \rangle} &= \frac{f^2 k_H^2 \text{KE}}{N^2 k_H^2 \text{PE}} = \frac{f^2 (N^2 - \omega^2)^2 (\omega^2 + f^2)}{N^4 (\omega^2 - f^2)^2} \\ &= \frac{(N^2 k_H^2 + 2f^2 k_z^2) f^2 k_z^4}{N^4 k_H^4 k^2} \end{aligned} \quad (4)$$

(Fofonoff 1969). The internal wave ratio exceeds one for $\omega < 1.7f$ and is less than unity for higher frequencies. Measured vertical wavenumber spectra for vertical shear $f\mathbf{V}_z$, horizontal buoyancy gradient $\nabla_H b$, and the ageostrophic acceleration $\mathbf{V}_{zi} = (-b_x + f v_z, -b_y - f u_z)$ are compared with GM spectra for these quantities in Fig. 14. The GM spectra have been low-pass filtered in horizontal wavenumber to remove the high horizontal wavenumbers suppressed by fitting over the surveys, and high-pass filtered in frequency to eliminate frequencies below $1.004f$, that is, below the near-inertial peak (D'Asaro and Perkins 1984).

If the fluctuations were purely geostrophic, the observed $f\mathbf{V}_z$ and $\nabla_H b$ spectra would be identical and the ageostrophic acceleration \mathbf{V}_{zi} spectra would vanish. While the measured horizontal buoyancy-gradient spectra contains more variance than the GM model, the vertical shear contains much more variance than the horizontal buoyancy gradient for both surveys, signifying a large near-inertial wave contribution.

This apparent contradiction with the conclusions of Figs. 9–13 can be reconciled by recognizing that the velocity and buoyancy fits contain contributions from horizontal scales at and larger than the surveys. If the horizontal wavenumber spectra are red with slopes more positive than -3 , then the observed vortex stretching $f b_z$ and vertical shear $f\mathbf{V}_z$ will be dominated by the energy-containing horizontal scales, which could

be larger than the survey, while the dominant contributions to relative vorticity ζN^2 and horizontal buoyancy gradient $\nabla_H b$ will be from scales comparable to the survey size. This highlights the limitations of using thermal wind to test for geostrophy in surveys when broadband horizontal internal wave fluctuations coexist on the same scales as the geostrophic flow. This problem does not exist for the Ertel vorticity test (Figs. 9–11), which isolates the Ertel vorticity-carrying part of the flow from internal waves.

4. Summary

Velocity and temperature profile surveys near Ampere Seamount have been used to examine three pairs of consistency relations for internal waves and geostrophy (Table 2): the Ertel potential vorticity, the ratio of horizontal divergence to relative vorticity, and thermal wind. A fourth consistency relation pair involving the ratio of potential to kinetic energy is investigated in a companion paper (Kunze 1993). Although unable to shed light on the controversial dynamics of fluctuations with vertical wavelengths less than 50 m (Müller et al. 1988; Kunze et al. 1990; Sherman and Pinkel 1991; D'Asaro and Morehead 1991; Lien and Müller 1991; Anderson and Pinkel 1993), the analysis reveals submesoscale Ertel vorticity anomalies with rms magnitudes of $0.2\text{--}0.4/N^2$ (Table 1) on vertical wavelengths as small as 50 m (Figs. 9 and 10), scales traditionally thought to be dominated by internal waves. These anomalies are an indisputable signature of geostrophic or nonlinear Ertel vorticity-carrying dynamics because internal waves and seamount-trapped waves (Brink 1990; Codiga 1993) have no Ertel vorticity fluctuations in the water column. Thus, Ertel vorticity-carrying dynamics coexists on the same scales as internal waves (at least in the vicinity of Ampere Seamount). Relative vorticities were less than $0.2f$ and the nonlinear Ertel vorticity terms were weak compared to the linear terms (Fig. 10; Table 1); therefore, the anomalies are in geostrophic balance.

As on basin scales, the Ertel vorticity signal over 4–7 km is dominated by vortex stretching $f b_z$ (Fig. 10); the relative vorticity ζN^2 was much weaker. The vortex-stretching signal is reminiscent of the density layering discussed in the internal wave/finestructure literature (Phillips 1971; Garrett and Munk 1971; McKean 1974; Eriksen 1978; Levine and Irish 1981). If the stretching were due to internal waves, it would be compensated by the vorticity ($f b_z = -\zeta N^2$). Since the vortex stretching dominates, it can be concluded that it is principally due to geostrophy. Moreover, where the vortex-stretching signal at a vertical wavenumber is attributable to geostrophy, so is the available potential energy since $\text{PE} = b_z^2 / (2k_z^2 N^2)$. This is commensurate with the partition of energy between internal waves and geostrophy found using the energy and length scale Burger numbers (Kunze 1993). From this,

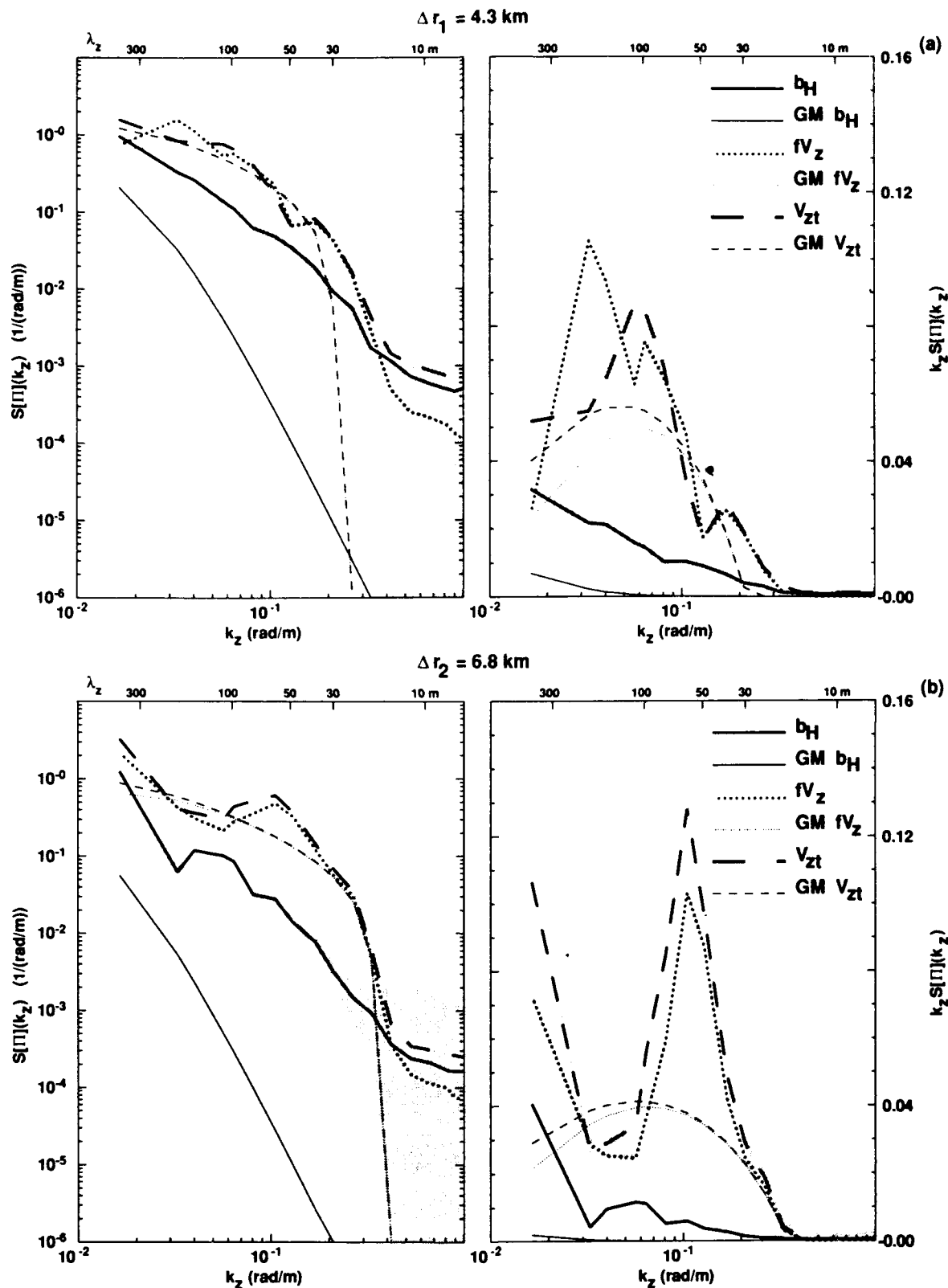


FIG. 14. Comparison of vertical wavenumber spectra of vertical shear fV_z (solid), horizontal buoyancy gradient $\nabla_H b \equiv b_H$ (dotted), and the ageostrophic acceleration $V_{zt} = (-b_x + f v_z, -b_y - f u_z)$ (dashed) with their GM model spectra low-pass filtered to remove horizontal wavenumbers suppressed by the fitting and high-pass filtered to remove frequencies lower than $1.004f$. All spectra have been normalized by fN_0 . If the observed fluctuations were purely geostrophic, the vertical shear and horizontal buoyancy gradient would be identical and the ageostrophic acceleration would vanish. The shear exceeds the buoyancy gradient, and the ageostrophic acceleration is of comparable magnitude to the shear in the observations, qualitatively consistent with the GM model.

TABLE 2. Consistency relations for internal wave and geostrophic fluctuations examined in this paper including the ratio of vortex stretching f/h_z to relative vorticity ζN^2 , the ratio of horizontal divergence ∇ to relative vorticity ζ , and the ratio of vertical shear f/l_z to horizontal buoyancy-gradient $\nabla_H b$ terms in the thermal wind balance.

Internal waves	Geostrophy
1. $\frac{f/h_z}{\zeta N^2} = -1$	$\frac{f/h_z}{\zeta N^2} = \frac{1}{R_L} = \left(\frac{fk_H}{Nk_z}\right)^2$
2. $\frac{\nabla}{\zeta^2} = \frac{\omega^2}{f^2} = \frac{N^2 k_H^2 + f^2 k_z^2}{f^2 k^2}$	$\frac{\nabla^2}{\zeta^2} = 0$
3. $\frac{\langle f^2 l_z^2 \rangle}{\langle (\nabla_H b)^2 \rangle} = \frac{f^2 k^2}{N^2 k_H^2 + 2f^2 k_z^2}$	$\frac{\langle f^2 l_z^2 \rangle}{\langle (\nabla_H b)^2 \rangle} = 1$

it might be thought that vortex stretching alone could be used to estimate Ertel vorticity down to scales of a few kilometers. However, given the uniqueness of the measurement site and that internal waves also contribute to submesoscale vortex stretching, relative vorticity must be measured to ensure that f/h_z is not compensated.

Spectra of the linear Ertel vorticity anomaly, $f/h_z + \zeta N^2$ (Fig. 11), contain more variance than do those of vortex stretching or relative vorticity alone. This suggests that the relative vorticity also is largely due to geostrophy since internal wave-induced vortex stretching and relative vorticity will balance each other ($|f/h_z + \zeta N^2| \ll |f/h_z| = |\zeta N^2|$) when nonlinear terms are small. Using (3), the horizontal wavelengths for the peak bands are 7–15 km. The geostrophic interpretation is borne out by comparison of vertical wavenumber spectra of relative vorticity and horizontal divergence (Fig. 13), which reveal vorticity in excess of divergence in peak bands, consistent with geostrophy but not internal waves (section 3d). Divergence dominates in other bands, consistent with internal wave but not geostrophic dynamics. Thus, there are contributions to the kinetic energy from both internal waves and geostrophy.

Using velocity profile surveys collected in the Beaufort Sea, D'Asaro and Morehead (1991) also reported evidence of kinetic energy associated with Ertel vorticity-carrying dynamics on horizontal scales less than a few kilometers at $\lambda_z = 40$ m. At $0.2 \text{ cm}^2 \text{ s}^{-2}$, their signal is comparable to the geostrophic kinetic energy found beside Ampere (Kunze 1993) and three times greater than that of high-frequency internal waves in the weak Arctic internal wave regime. This part of the Arctic is known to contain many small eddies (Manley and Hunkins 1985; D'Asaro 1988a), which D'Asaro (1988b) argues are generated by frictional torques in Barrow Canyon.

In contrast, Kunze et al. (1990), Sherman and Pinkel (1991), and Anderson and Pinkel (1993) concluded that finescale ($\lambda_z \leq 10$ m) shear is dominated by near-inertial waves based on measurements 1000 km off the

coast of California. Lien and Müller (1992b) find that fluctuations with $\lambda_z > 70$ m are consistent with internal waves in the Sargasso Sea. Thus, it is too soon to tell whether the results found here are typical of the ocean or due to topography.

5. Discussion

The finding of strong Ertel vorticity anomalies $\sim O(0.3 f N^2)$ beside Ampere Seamount raises the questions of how they were generated and whether they are typical of the ocean pycnocline or due to the proximity of topography (Fig. 1). Four formation mechanisms seem plausible: (i) transfer of variance from lower horizontal wavenumbers as part of the potential enstrophy cascade to high k_H of geostrophic turbulence (Charney 1971), (ii) dissipative turbulence and mixing in the pycnocline (Riley et al. 1981), (iii) detrainment of the late-winter mixed layer followed by subduction (e.g., Stommel 1979; Marshall et al. 1993), and (iv) intensified mixing processes on topography. These are discussed below in order of increasing plausibility.

If interpreted as geostrophic turbulence, the Ertel vorticity anomalies must be produced by eddy stirring of the large-scale background gradients of $f N^2$. This implies turbulent stirring lengths $\delta \Pi / |\nabla_H f N^2|$ of thousands of kilometers based on the rms Ertel vorticity anomaly $\delta \Pi \approx 0.3 f N^2$ and the large-scale background gradients of $f N^2$ due to the β effect and gyre-scale circulation (McDowell et al. 1982; Keffer 1985). The observations occupy $\sigma_\theta = 26.7$ – 27.1 (Fig. 4), close to the homogenized pool described by McDowell et al. (1982), where Rhines and Young (1982) predict vanishing eddy potential energy; however, stronger $f N^2$ gradients $\sim O(\beta N_\theta^2)$ exist to the north. Stirring lengths of thousands of kilometers are unrealistically large, indicating that the observed signal is not representative of the high-wavenumber end of the potential enstrophy cascade.

Because turbulent dissipation and mixing are weak and confined to vertical scales of a few meters in the ocean interior, Ertel vorticity anomalies produced by dissipative turbulence in the pycnocline should likewise be weak and confined to small vertical scales. Given typical dissipation rates $\epsilon \approx 10^{-9} \text{ W kg}^{-1}$ (Moum and Osborn 1986; Gregg 1987; Gregg 1989; Yamazaki et al. 1990), mixing efficiencies less than 0.2 (Itsweire et al. 1986), and assuming equal generation of internal waves and Ertel vorticity-carrying fluctuations, an upper bound for the rate of energy transfer to Ertel vorticity anomalies is $\sim 0.3 \text{ cm}^2 \text{ s}^{-2} \text{ day}^{-1}$. This is sufficient to fill the $\sim 1 \text{ cm}^2 \text{ s}^{-2}$ in the Ertel vorticity anomalies (Kunze 1993) in under a week (lower bound). However, to do so would require many mixing events, each of only a few buoyancy periods duration, to be cumulative. While Gregg et al. (1986) found that one turbulent patch associated with a near-inertial wave packet persisted for many days, most turbulence events

appear to occur randomly throughout the water column.

Random turbulence will erode Ertel vorticity anomalies rather than create them. (Erosion times will be much longer than the above-quoted formation times because most of the turbulent dissipation is supplied by small-scale internal waves.) An eddy viscosity of $\nu = \epsilon / U^2 \leq \epsilon / (4N^2) \approx 0.1 \times 10^{-4} \text{ m}^2 \text{ s}^{-1}$ can be deduced assuming that internal wave-induced turbulence acts to smooth larger-scale shear as well as the unstable small-scale shear; this is a reasonable assumption if turbulence production is driven by internal wave-wave interactions (Henyey et al. 1986) uncorrelated with the Ertel vorticity-carrying flow. The above eddy viscosity implies a decay time (Gill 1981) of ~ 10 yr for $\lambda_z = 400$ m and 2–3 months for $\lambda_z = 50$ m. Corresponding advection length scales are 20 000 and 400 km for a 5-cm s^{-1} current. Thus, the observed 50-m vertical wavelength feature (Figs. 9 and 10) will not be long-lived or of distant origin.

Double diffusion can also create stretching vorticity in the form of staircases and thermohaline intrusions but the associated horizontal velocity fields are much weaker ($< 1 \text{ cm s}^{-1}$) than those observed.

An ironclad case cannot be made against production by microscale dissipative turbulence in the pycnocline. However, given that the strongest turbulent dissipation and mixing occur at the surface (Schmitt and Olson 1985; Shay and Gregg 1986) and benthic boundaries (Nabatov and Ozmidov 1988; Toole and Schmitt 1992, personal communication), these might be argued to be the most likely sites for generation of submesoscale Ertel vorticity perturbations.

The retreat of the winter mixed layer is likely to leave behind "granularity" in Ertel vorticity just as it does in tracers (Jenkins 1982). The density range $\sigma_\theta = 26.7\text{--}27.1$ (Fig. 4) is about 1000 km from its winter outcrop (McDowell et al. 1982; Keffer 1985). Unlike internal waves, Ertel vorticity anomalies cannot propagate because they are tied to water parcels. They can only be carried into the ocean interior by relatively slow low-frequency advection. Because of weak dissipation in the interior, anomalies with $\lambda_z > 100$ m might survive relatively intact as they are subducted and swept around the gyre. However, if the arguments about erosion by dissipative turbulence already presented are correct, detrainment cannot explain the 50-m wavelength anomaly at 400-m depth as the measurements were collected six months after retreat of the winter mixed layer, twice the decay time quoted above. Given the uncertainties in the effects of turbulence, a more convincing argument might be that buoyancy forcing in late winter would create θ , S anomalies as well and these are absent between depths of 150 and 600 m. Therefore, detrainment in late winter can be ruled out.

Generation of Ertel vorticity anomalies on the flanks of Ampere Bank or other nearby seamounts to the northeast (Fig. 1) followed by shedding or injection

into the pycnocline (Armi 1978; Geyer and Signell 1990; Prater 1992) is the most plausible formation mechanism on the grounds of both proximity of Ampere Seamount and the intensity of irreversible processes at topography. Observed dissipation rates in stratified waters on the flanks and summits of seamounts are 100–1000 times greater than typical pycnocline dissipation rates (Osborn 1978; Nabatov and Ozmidov 1988; Padman and Dillon 1991; Toole and Schmitt 1992, personal communication), reducing formation times to fractions of a day.

Evidence for benthic boundary-layer detachment near topography has been reported by Armi (1978), Osborn (1978), Hogg et al. (1978), and Nabatov and Ozmidov (1988). Rossby numbers of at least 0.3 are revealed by the drifter tracks (Fig. 3). Laboratory experiments in a stratified fluid produce vortex shedding for Rossby numbers greater than 0.03 (Zhang and Boyer 1993). However, the numerical simulations of Smolarkiewicz and Rotunno (1989) demonstrate that inviscid flow can produce "vortices" in the wake of a seamount that are, in fact, manifestations of nonlinear internal waves with no Ertel vorticity signal, raising doubts about interpretations of "eddy-shedding" laboratory experiments. Bormans and Garrett (1989) suggest that a necessary criterion for flow separation is that $U/(fr) > 1$, where r is the radius of curvature of the topography. For the observed flow speeds of $5\text{--}10 \text{ cm s}^{-1}$, flow separation would require a radius of curvature less than 1 km. Features of this size can be seen on the 200- and 500-m isobaths in Figs. 2 and 3.

In conclusion, within a few kilometers of Ampere Bank, internal waves and geostrophic fluctuations coexist on wavelengths $\lambda_z = 50\text{--}400$ m and $\lambda_H \approx 7\text{--}15$ km (see also Kunze 1993). Traditionally, these scales have been interpreted as internal waves. Vortex stretching (strain) and available potential energy are dominated by geostrophy, while both internal waves and geostrophic motions contribute to the horizontal kinetic energy. Despite these results, it is premature to assign a significant contribution from Ertel vorticity-carrying dynamics to pycnocline submesoscale and finescale fluctuations because the most plausible source for the observed Ertel vorticity variance is flow interaction with local topography. The strength of Ertel vorticity-carrying fluctuations in the main pycnocline away from topography remains to be determined. Indirect evidence for subinertial shear comes from horizontal diffusion in the ocean being much higher [$\sim 3 \text{ m}^2 \text{ s}^{-1}$ (Ledwell et al. 1993)] than can be accounted for by internal wave shear dispersion [$\sim 0.01 \text{ m}^2 \text{ s}^{-1}$ (Young et al. 1982)]. Probing the dynamics of the submesoscale and finescale promises a rewarding area for research in the coming decade.

Acknowledgments. We thank John Dunlap for his assistance in modifying Eric D'Asaro's XCP data acquisition program to acquire XBT data, Maureen

Kennelly for handling the logistics, Tom Lehman for the CTD work, and Captain Paul Howland and the crew of *Oceanus* for their able assistance. The authors gained valuable insights from Peter Müller, Ren-Chieh Lien, Eric D'Asaro, Larry Armi, Mark Prater, Bill Dewar, and Frank Henyey. Comments by Chris Garrett, Dan Kelley, and an anonymous reviewer have helped clarify the text. The first author would like to acknowledge his debt to Jack Schratte, physicist and teacher, who died 25 March 1993. This work was supported by ONR Grant N00014-90-J-1100.

APPENDIX A

The Low-Pass Filtered GM Spectrum

The GM internal wave model spectrum (Garrett and Munk 1979; Munk 1981) is usually posed in terms of intrinsic frequency ω and vertical wavenumber k_z (or mode number j) and is separable in these variables. For comparison with the XCP survey data in Figs. 12 and 13, the model spectrum needs to be expressed in terms of horizontal and vertical wavenumbers, then low-pass filtered in horizontal wavenumber to eliminate the high horizontal wavenumbers that are suppressed in making horizontal least-squares fits. This is particularly important for the horizontal divergence $\nabla = (\mathbf{k}_H \cdot \mathbf{V}_H)$ and relative vorticity $\zeta = (\mathbf{k}_H \times \mathbf{V}_H)$, which are not red in horizontal wavenumber but have much of their variance at small horizontal scales.

Using the approximate internal wave dispersion relation valid for $\omega \ll N$, which should apply for the horizontal scales resolved by the survey,

$$\omega = \frac{\sqrt{f^2 k_z^2 + N^2 k_H^2}}{k_z}. \quad (\text{A1})$$

The GM76 spectra (Cairns and Williams 1976) for horizontal divergence and relative vorticity can be expressed as

$$S[\nabla](k_H, k_z) = E_o f^2 N_o b^2 \frac{k_H^2}{(f^2 k_z^2 + N^2 k_H^2)} \frac{k_z k_z^*}{(k_z + k_z^*)^2} \quad (\text{A2})$$

$$S[\zeta](k_H, k_z) = E_o f^3 N_o b^2 \times \frac{k_H^2}{(f^2 k_z^2 + N^2 k_H^2)^2} \frac{k_z^3 k_z^*}{(k_z + k_z^*)^2}, \quad (\text{A3})$$

where the dimensionless energy level $E_o = 6.3 \times 10^{-5}$, a typical upper-pycnocline buoyancy frequency $N_o = 5.2 \times 10^{-3} \text{ s}^{-1}$, $b = 1300 \text{ m}$, and the scale wavenumber $k_z^* = (\pi/b)(N/N_o)j^*$, where $j^* = 3$ at mid-latitudes. Integrating (A2) and (A3) from $k_H = 0$ to a high-wavenumber cutoff k_{Hc} provides a low-pass-filtered spectra in terms of vertical wavenumber k_z and the cutoff horizontal wavenumber k_{Hc} .

$$S[\nabla](k_z) = E_o f^2 \frac{N_o}{N} b^2 (\chi - \arctan(\chi)) \frac{k_z^2 k_z^*}{(k_z + k_z^*)^2} \quad (\text{A4})$$

$$S[\zeta](k_z) = \frac{E_o}{2} f^2 \frac{N_o}{N} b^2 \times \left(\arctan(\chi) - \frac{\chi}{\chi^2 + 1} \right) \frac{k_z^2 k_z^*}{(k_z + k_z^*)^2}, \quad (\text{A5})$$

where the cutoff aspect ratio $\chi = (N k_{Hc} / f k_z)$.

APPENDIX B

Low-Pass and Contamination Response Functions for a Cross-shaped Array

An array containing a finite number of elements cannot determine the horizontal gradient exactly. Such an array low passes scales smaller than the element separation, but imperfectly, so that there is some contamination by higher wavenumber variance. In particular, for a horizontal array, relative vorticity will be

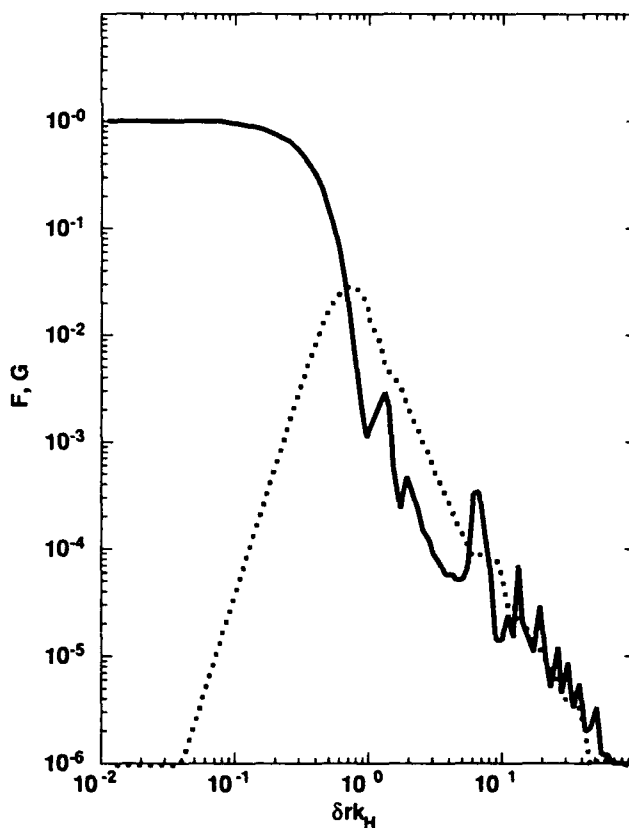


FIG. B1. The low-pass attenuation F (solid) and contamination G (dotted) response functions for a cross-shaped array containing 12 elements per leg as a function of normalized horizontal wavenumber $\delta r k_H$, where δr is the separation between adjacent elements. The low-pass attenuation response function is one for $\delta r k_H \leq 0.2$ and falls off steeply for higher wavenumbers. The contamination function G has a peak of 0.03 at $\delta r k_H = 0.7$.

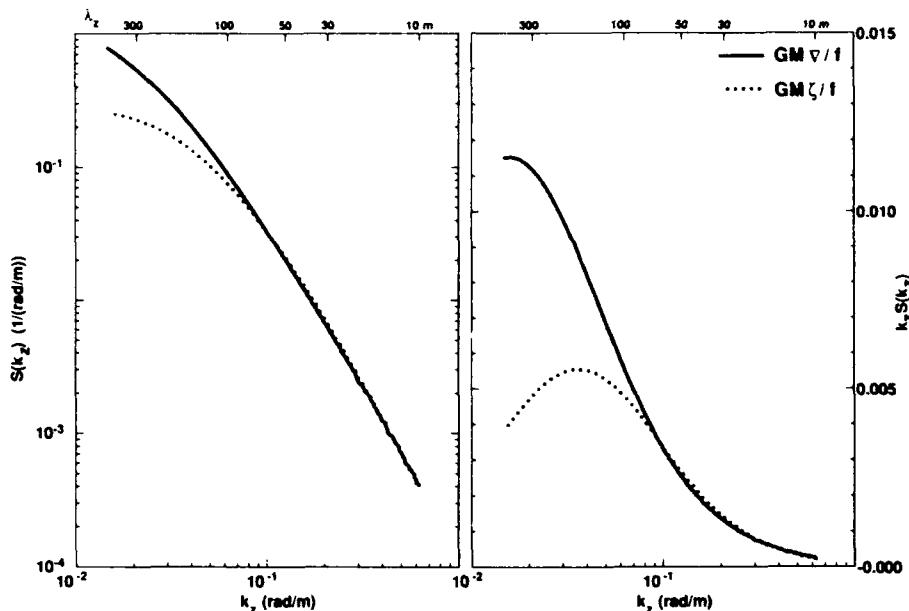


FIG. B2. Vertical wavenumber spectra of GM model horizontal divergence (solid) and relative vorticity (dot) filtered with the low-pass attenuation and contamination response functions for a cross-shaped array with 12 elements per leg and $\delta r = 0.3$ km. The spectra are displayed in both log-log (left) and variance-preserving (right) formats. The filtered vorticity spectrum exceeds the divergence spectra by $\sim 10\%$ for $\lambda_z = 20$ –50 m.

contaminated by horizontal divergence and vice versa (Lien and Müller 1992b). Lien (1992, personal communication) has formulated the low-pass attenuation and contamination array response functions for a cross-shaped survey. His formulation is reproduced here with his kind permission. The low-pass attenuation response function is

$$F(k_H) = \left(\frac{6}{M(M^2 - 1)k_H\delta r} \right)^2 \sum_{j=1}^M \sum_{k=1}^M (2j - M - 1) \\ \times (2k - M - 1) \times \left\{ J_0((k - j)k_H\delta r) - J_2((k - j)k_H\delta r) - \sin \left(2 \arctan \left(- \frac{2k - M - 1}{2j - M - 1} \right) \right) \right. \\ \left. \times J_2 \left(\sqrt{(2j - M - 1)^2 + (2k - M - 1)^2} k_H\delta r / 2 \right) \right\} \quad (B1)$$

and the contamination array response function

$$G(k_H) = 2 \left(\frac{6}{M(M^2 - 1)k_H\delta r} \right)^2 \\ \times \sum_{j=1}^M \sum_{k=1}^M (2j - M - 1)(2k - M - 1) \\ \times J_0((k - j)k_H\delta r) - F(k_H), \quad (B2)$$

where M is the number of elements in each leg, k_H the horizontal wavenumber of interest, and δr the separation between adjacent elements.

The two filter functions are displayed as functions of normalized horizontal wavenumber $k_H\delta r$ in Fig. B1 for $M = 12$. The low-pass function F (solid curve) is one for $k_H\delta r < 0.2$, and falls off steeply for higher wavenumbers. The contamination function G rises above the low-pass response function and peaks at $G_{\max} = 0.03$ for slightly higher $k_H\delta r = 0.7$ so that relative vorticity (horizontal divergence) estimates will be contaminated by horizontal divergence (relative vorticity) from smaller wavelengths.

Figure B2 displays the filtered, contaminated GM spectra for horizontal divergence and relative vorticity

$$\hat{S}[\nabla](k_z) = \int \{ S[\nabla](k_z, k_H) \cdot F(k_H) + S[\zeta](k_z, k_H) \cdot G(k_H) \} dk_H \\ \hat{S}[\zeta](k_z) = \int \{ S[\zeta](k_z, k_H) \cdot F(k_H) + S[\nabla](k_z, k_H) \cdot G(k_H) \} dk_H \quad (B3)$$

with $M = 14$ and $\delta r = 0.3$ km appropriate for survey 1. The vorticity spectra will be more contaminated by divergence than the divergence by the vorticity because the GM divergence spectra contain more variance at high horizontal wavenumber. The filtered, contaminated GM spectra differ from the simple boxcar filter used for Fig. 13 only in that the vorticity exceeds the divergence spectra by 10% at high vertical wavenum-

bers ($\lambda_z < 60$ m). We caution that a cross-shaped survey is a suboptimal sampling pattern, equivalent to four points on a circle (Lien 1992, personal communication), and succeeds in this paper only because the horizontal divergence and relative vorticity are of comparable magnitude. For smaller surveys sampling the scales for which internal wave horizontal divergence greatly exceeds the relative vorticity, the optimal array pattern would be a circle or a square grid containing at least nine stations.

REFERENCES

- Anderson, S. P., and R. Pinkel, 1993: Observations of semi-Lagrangian velocity finestructure. *J. Phys. Oceanogr.*, submitted.
- Armi, L., 1978: Some evidence of boundary mixing in the deep ocean. *J. Geophys. Res.*, **83**, 1971–1979.
- Bormans, M., and C. Garrett, 1989: A simple criterion for gyre formation by the surface outflow from a strait, with application to the Alboran Sea. *J. Geophys. Res.*, **94**, 12 637–12 644.
- Brink, K. H., 1990: On the generation of seamount-trapped waves. *Deep-Sea Res.*, **37**, 1569–1582.
- Briscoe, M. G., 1977: On current finestructure and moored current-meter measurements of internal waves. *Deep-Sea Res.*, **24**, 1121–1131.
- Cairns, J. L., and G. O. Williams, 1976: Internal wave observations from a midwater float. 2. *J. Geophys. Res.*, **81**, 1943–1950.
- Charney, J. G., 1971: Geostrophic turbulence. *J. Atmos. Sci.*, **28**, 1087–1095.
- Codiga, D. L., 1993: Laboratory realizations of stratified seamount-trapped waves. *J. Phys. Oceanogr.*, **23**, 2053–2071.
- D'Asaro, E. A., 1988a: Observations of small eddies in the Beaufort Sea. *J. Geophys. Res.*, **93**, 6669–6684.
- , 1988b: Generation of submesoscale vortices: A new mechanism. *J. Geophys. Res.*, **93**, 6685–6693.
- , and M. D. Morehead, 1991: Internal waves and velocity finestructure in the Arctic Ocean. *J. Geophys. Res.*, **96**, 12 725–12 738.
- , and H. Perkins, 1984: A near-inertial internal wave spectrum for the Sargasso Sea in late summer. *J. Phys. Oceanogr.*, **14**, 489–505.
- Efron, B., and G. Gong, 1983: A leisurely look at the bootstrap, the jackknife and cross-validation. *Amer. Stat.*, **37**, 36–48.
- Eriksen, C. C., 1978: Measurements and models of finestructure, internal gravity waves, and wave breaking in the deep ocean. *J. Geophys. Res.*, **83**, 2989–3009.
- Ertel, H., 1942: Ein neuer hydrodynamischer Wirbelsatz. *Meteorol. Z.*, **59**, 277–281.
- Fofonoff, N. P., 1969: Spectral characteristics of internal waves in the ocean. *Deep-Sea Res.*, **16** (Suppl.), 58–71.
- Garrett, C. J. R., and W. Munk, 1971: Internal wave spectra in the presence of finestructure. *J. Phys. Oceanogr.*, **1**, 196–202.
- , and —, 1979: Internal waves in the ocean. *Annu. Rev. Fluid Mech.*, **11**, 339–369.
- Geyer, W. R., and R. Signell, 1990: Measurements of tidal flow around a headland with a shipboard acoustic Doppler current profiler. *J. Geophys. Res.*, **95**, 3189–3197.
- Gill, A. E., 1981: Homogeneous intrusions in a rotating stratified fluid. *J. Fluid Mech.*, **103**, 275–295.
- Gregg, M. C., 1987: Diapycnal mixing in the thermocline: A review. *J. Geophys. Res.*, **92**, 5249–5286.
- , 1989: Scaling turbulent dissipation in the thermocline. *J. Geophys. Res.*, **94**, 9686–9698.
- , E. A. D'Asaro, T. J. Shay, and N. Larson, 1986: Observations of persistent mixing and near-inertial internal waves. *J. Phys. Oceanogr.*, **16**, 856–885.
- Haynes, P. H., and M. E. McIntyre, 1987: On the evolution of vorticity and potential vorticity in the presence of diabatic heating and frictional or other forces. *J. Atmos. Sci.*, **44**, 828–841.
- Heney, F. S., J. Wright, and S. M. Flatte, 1986: Energy and action flow through the internal wave field. *J. Geophys. Res.*, **91**, 8487–8495.
- Herring, J. A., and O. Metais, 1989: Numerical experiments in forced stably-stratified turbulence. *J. Fluid Mech.*, **202**, 97–115.
- Hogg, N. G., E. J. Katz, and T. B. Sanford, 1978: Eddies, islands and mixing. *J. Geophys. Res.*, **83**, 2921–2938.
- Holloway, G., 1983: A conjecture relating oceanic internal waves and small-scale processes. *Atmos.-Ocean*, **31**, 107–122.
- Hoskins, B. J., M. E. McIntyre, and R. W. Robertson, 1985: On the use and significance of isentropic potential vorticity maps. *Quart. J. Roy. Meteor. Soc.*, **111**, 877–946.
- Itsweire, E. C., K. N. Helland, and C. W. van Atta, 1986: The evolution of grid-generated turbulence in a stably stratified fluid. *J. Fluid Mech.*, **162**, 299–338.
- Jenkins, W. J., 1982: On the climate of a subtropical ocean gyre: Decade time-scale variations in water-mass renewal in the Sargasso Sea. *J. Mar. Res.*, **40** (Suppl.), 265–290.
- Keffer, T., 1985: The ventilation of the world's oceans: Maps of the potential vorticity field. *J. Phys. Oceanogr.*, **15**, 509–523.
- Kennelly, M. A., M. D. Prater, J. H. Dunlap, E. Kunze, and T. B. Sanford, 1989: XCP data from the Gulf of Cadiz Expedition: R/V Oceanus Cruise 202. Tech. Rep. 8925, Applied Physics Lab, University of Washington, Seattle, WA, 206 pp.
- Kunze, E., 1993: Submesoscale dynamics near a seamount. Part II: The partition of energy between internal waves and geostrophy. *J. Phys. Oceanogr.*, **23**, 2589–2601.
- , M. G. Briscoe, A. J. Williams III, 1990: Interpreting shear and strain finestructure from a neutrally-buoyant float. *J. Geophys. Res.*, **95**, 18 111–18 125.
- Ledwell, J. R., A. J. Watson, and C. S. Law, 1993: Evidence of slow mixing across the pycnocline from an open-ocean tracer-release experiment. *Nature*, **364**, 701–703.
- Lelong, M.-P., and J. J. Riley, 1992: Internal wave-vortical mode interactions in strongly-stratified flows. *J. Fluid Mech.*, **232**, 1–19.
- Levine, M. D., and J. D. Irish, 1981: A statistical description of temperature finestructure in the presence of internal waves. *J. Phys. Oceanogr.*, **11**, 676–691.
- Lien, R.-C., and P. Müller, 1991: Estimates of small-scale horizontal divergence and relative vorticity in the ocean. *Dynamics of Oceanic Internal Gravity Waves, Proc. 'Aha Huliko'a Hawaiian Winter Workshop, 'Aha Huliko'a, Hawaii, Hawaii Geophys. Inst.*, 143–155.
- , and —, 1992a: Consistency relations for gravity and vortical modes in the ocean. *Deep-Sea Res.*, **39**, 1595–1612.
- , and —, 1992b: Normal-mode decomposition of small-scale oceanic motions. *J. Phys. Oceanogr.*, **22**, 1583–1595.
- Lilly, D. K., 1983: Stratified turbulence and the mesoscale variability of the atmosphere. *J. Atmos. Sci.*, **40**, 749–760.
- Marshall, J. C., A. J. G. Nurser, and R. G. Williams, 1993: Inferring the subduction rate and period over the North Atlantic. *J. Phys. Oceanogr.*, **23**, 1315–1329.
- McDowell, S., P. Rhines, and T. Keffer, 1982: North Atlantic potential vorticity and its relation to the general circulation. *J. Phys. Oceanogr.*, **12**, 1417–1436.
- McKean, R. S., 1974: Interpretation of internal wave measurements in the presence of finestructure. *J. Phys. Oceanogr.*, **4**, 200–213.
- Manley, T. O., and K. Hunkins, 1985: Mesoscale eddies of the Arctic Ocean. *J. Geophys. Res.*, **90**, 4911–4930.
- Moum, J. N., and T. R. Osborn, 1986: Mixing in the main thermocline. *J. Phys. Oceanogr.*, **16**, 1250–1259.
- Müller, P., 1984: Smallscale vortical motions. *Internal Gravity Waves and Smallscale Turbulence, Proc. 'Aha Huliko'a Hawaiian Winter Workshop, 'Aha Huliko'a, Hawaii, Hawaiian Inst. Geophys.*, 249–262.
- , D. J. Olbers, and J. Willebrand, 1978: The IWEX spectrum. *J. Geophys. Res.*, **83**, 479–500.
- , R.-C. Lien, and R. Williams, 1988: Estimates of potential vor-

- ticity at small scales in the ocean. *J. Phys. Oceanogr.*, **18**, 401-416.
- Munk, W., 1981: Internal waves and small-scale processes. *Evolution of Physical Oceanography*. B. A. Warren and C. Wunsch, Eds., The MIT Press, 264-291.
- Nabatov, V. N., and R. V. Ozmidov, 1988: Study of turbulence above seamounts in the Atlantic Ocean. *Oceanology*, **28**, 161-166.
- Osborn, T. R., 1978: Measurements of energy dissipation adjacent to an island. *J. Geophys. Res.*, **83**, 2939-2957.
- Padman, L., and T. M. Dillon, 1991: Turbulent mixing near the Yermak Plateau during the Coordinated Eastern Arctic Experiment. *J. Geophys. Res.*, **96**, 4769-4782.
- Pedlosky, J., 1979: *Geophysical Fluid Dynamics*. Springer-Verlag, 624 pp.
- Phillips, O. M., 1971: On spectra measured in an undulating layered medium. *J. Phys. Oceanogr.*, **1**, 1-6.
- Pollard, R. T., and L. A. Regier, 1992: Vorticity and vertical circulation at an ocean front. *J. Phys. Oceanogr.*, **22**, 609-625.
- Prater, M. D., 1992: Observations and hypothesized generation of a Meddy in the Gulf of Cadiz. APL-UW Tech. Rep. TR9210, Appl. Phys. Lab., University of Wash., Seattle, 132 pp.
- Rhines, P., and W. Young, 1982: Homogenization of potential vorticity in planetary gyres. *J. Fluid Mech.*, **122**, 347-368.
- Riley, J. J., R. W. Metcalfe, and M. A. Weissman, 1981: Direct numerical simulations of homogeneous turbulence in density-stratified fluids. *Nonlinear Properties of Internal Waves*, Vol. 76, B. J. West, Ed., Amer. Inst. Phys., 79-112.
- Sanford, T. B., R. G. Drever, J. H. Dunlap, and E. A. D'Asaro, 1982: Design, operation and performance of an expendable temperature and velocity profiler (X1VP). Tech. Rep. 8110, Appl. Phys. Lab., University of Washington, 83 pp.
- Schmitt, R. W., and D. B. Olson, 1985: Wintertime convection in warm-core rings: Thermocline ventilation and formation of mesoscale lenses. *J. Geophys. Res.*, **90**, 8823-8837.
- Shay, T. J., and M. C. Gregg, 1986: Convectively-driven turbulence mixing in the upper ocean. *J. Phys. Oceanogr.*, **16**, 1777-1798.
- Sherman, J. T., and R. Pinkel, 1991: Estimates of the vertical wave-number-frequency spectra of vertical shear and strain. *J. Phys. Oceanogr.*, **21**, 292-303.
- Signell, R. P., and W. R. Geyer, 1991: Transient eddy formation around headlands. *J. Geophys. Res.*, **96**, 2561-2575.
- Smolarkiewicz, P. K., and R. Rotunno, 1989: Low Froude number flow past three-dimensional obstacles. Part I: Baroclinically-generated lee vortices. *J. Atmos. Sci.*, **46**, 1154-1164.
- Staquet, C., and J. J. Riley, 1989: A numerical study of a stably-stratified mixing layer. *Turbulent Shear Flows*, **6**, Springer-Verlag, Berlin, 381-397.
- Stommel, H., 1979: Determination of water-mass properties of water pumped down from the Ekman layer to the geostrophic flow below. *Proc. Natl. Acad. Sci., U.S.*, **76**, 3051-3055.
- Yamazaki, H., R. G. Lueck, and T. Osborn, 1990: A comparison of turbulence data from a submarine and a vertical profiler. *J. Phys. Oceanogr.*, **20**, 1778-1786.
- Young, W. R., P. B. Rhines, and C. J. R. Garrett, 1982: Shear-flow dispersion, internal waves, and horizontal mixing in the ocean. *J. Phys. Oceanogr.*, **12**, 515-527.
- Zhang, X., and D. L. Boyer, 1993: Laboratory study of rotating, stratified, oscillatory flow over a seamount. *J. Phys. Oceanogr.*, **23**, 1122-1141.

Accession For	
NTIS SRA&I	<input checked="" type="checkbox"/>
DTIC TAB	<input type="checkbox"/>
Unannounced	<input type="checkbox"/>
Justification	
By	
Distribution	
Availability Codes	
Dist	Attn. and/or Special
A-1	20